In Situ Generated Turbostratic 2D Graphite: A New Way to Obtain High-Performance Self-Lubricating Iron-Based Composites

3

Jose Daniel Biasoli de Mello, Cristiano Binder,
Sonia Maria Hickel Probst, and Aloisio Nelmo Klein

Contents

Abstract

The production of self-lubricating composites containing second phase particles is one of the most promising choices for controlling friction and wear in energy efficient modern systems. Initially, we present a new microstructural model/ processing route able to produce a homogeneous dispersion of in situ generated, discrete, solid lubricant particles in the volume of sintered composites. The high mechanical and tribological performances of the composites are a result of the combination of matrix mechanical properties and structural parameters, such as the degree of continuity of the metallic matrix, the nature, the amount, and the lubricant particle size and shape which determine the mean free path between

J. D. B. de Mello (✉) · C. Binder · S. M. H. Probst · A. N. Klein
Laboratório de Materiais, Departamento de Engenharia Mecânica, Universidade Federal de Santa Catarina, Florianópolis, SC, Brazil
e-mail: ltm-demello@ufu.br

73

solid lubricant particles and the active area covered by each lubricant particles. This new route was achieved by in situ formation of graphite nodules due to the dissociation of a precursor (SiC particles) mixed with metallic matrix powders during the feedstock preparation. Thermal debinding and sintering were performed in a single thermal cycle using a plasma-assisted debinding and sintering (PADS) process. Nodules of graphite (size ≤20 μm) presenting a nanostructured stacking of graphite foils with thickness of a few nanometers were obtained. Micro-Raman spectroscopy indicated that the graphite nodules are composed of a so-called turbostratic 2D graphite which has highly misaligned graphene planes separated by large interlamellae distance. The large interplanar distance and misalignment among the graphene foils has been confirmed by transmission electron microscopy and is, probably, the origin of the remarkably low dry friction coefficient (0.06). The effects of precursor content (0 to 5 wt% SiC) and of sintering temperature (1100 °C, 1150 °C and 1200 °C) on tribolayer durability and average friction coefficient in the lubricious regime (μ < 0.2) are presented and discussed. In addition, the effect of the metallic matrix composition (Fe-C; Fe-C-Ni; Fe-C-Ni-Mo) is presented. Friction coefficient decreased and durability drastically increased with the amount of graphite formed during sintering, whereas friction coefficient was little affected by sintering temperature. However, the durability of the tribolayer was greatly increased when lower sintering temperatures were used. The addition of alloying elements considerably reduced wear rate and friction of specimens and counter-bodies. Friction coefficient values as low as 0.04 were obtained for the Fe-C-Ni-Mo composites. We also analyzed the effect of precursor content and of sintering temperature on the tribological behavior under constant normal load sliding tests. Again, the presence of graphite nodules significantly reduced the friction coefficients and wear rates, whereas the sintering temperature hardly affected these parameters. The results were compared with those caused by other forms of graphite (nodules in nodular cast iron and powder graphite) and were discussed in terms of the crystalline structure of the analyzed graphite using micro-Raman spectroscopy. Chemical analyses of the wear scars using scanning electron microscopy (SEM – EDX) and Auger electron spectroscopy (AES) showed a tribolayer that was composed predominantly of carbon and oxygen. This tribolayer is removed and restored during sliding and is continuously replenished with graphite. Finally, the strong effect of surface finishing is presented and discussed.

3.1   Introduction

The crucial need for more energy efficient mechanical systems exacted the change in the severity of the tribological contacts, increasing operational failure for traditional designs. In this context, the tribology of critical contacts and possible new contact materials are under intense research investigation [1–3]. Furthermore, the interfaces in contact in these modern systems must be able to withstand severe operating

conditions caused by the tendency of using smaller clearances and increased speeds to achieve higher efficiency [4]. In addition, the state of lubrication in many components is unknown and usually operates in the boundary and mixed lubrication regimes [5].

In particular, solid lubrication and solid lubricants are one of the most promising choices for controlling friction and wear in energy efficient modern systems. A combination of solid and liquid lubrication is also feasible and may have a beneficial synergistic effect on the friction and wear performance of sliding surfaces, in particular in the elasto-hydrodynamic regime of lubrication [6].

Several inorganic materials (e.g., transition-metal, graphite, hexagonal boron nitride, boric acid) can provide excellent lubrication [7–10]. Most of these solids owe their lubricity to a lamellar or layered crystal structure. A few others (e.g., soft metals, polytetrafluoroethylene, polyimide, certain oxides and rare-earth fluorides, diamond and diamond-like carbons (DLC), fullerenes) can also provide lubrication although they do not have a layered crystal structure [8–10].

In spite of considerable research development, through more than 2000 published papers during the past 25 years, there exists no single solid lubricant that can provide both low friction and low wear over broad operational conditions [11]. In order to achieve a combination of high wear resistance, high load support, and low friction coefficient, a multifunctional production process combining purpose-oriented phases can be applied [12, 13].

The increasingly multifunctional needs and more stringent operating conditions envisioned for future mechanical systems will certainly make solid tribological materials and advanced coatings far more important. [14].

To meet the increasing tribological needs of these advanced systems, researchers are constantly exploring new materials and developing novel coatings. As a result, great strides have been made in recent years in the fabrication and diverse utilization of new tribomaterials and coatings that are capable of satisfying the multifunctional needs of more advanced mechanical systems [14].

Accordingly to Erdemir [15], solid lubricants can be applied to a tribological surface in a variety of forms. The oldest and simplest method is to sprinkle, rub, or burnish the fine powders of solid lubricants. Certain solid lubricants have been blended in an aerosol carrier and sprayed directly onto the surfaces to be lubricated. Solid lubricant powders can be strongly bonded to a surface by appropriate adhesives and epoxy resins to provide longer wear life [12]. Powders and nano-particles made of solid lubricants have been mixed with oils and greases to achieve improved lubrication under extreme pressure and high temperature conditions [16–21]. In most modern applications, thin films of solid lubricants, generally deposited onto surfaces by advanced vacuum deposition processes, are preferred to powders or bonded forms. In this case, the durability of the lubricious effect is limited due to the finite lubricant film thickness. To increase durability of these films, a self-replenishment or resupply mechanism is needed but is very difficult to obtain [15].

In this context the production of self-lubrication composites containing second phase particles incorporated into the volume of the material appears to be a

promising solution [11, 22, 23]. Indeed, self-lubricating composites have been available for a long time and are used rather extensively by industry to combat friction and wear in a variety of sliding, rolling, and rotating bearing applications [15].

Composite self-lubricating components have been used for several decades in household and office light equipments such as printers, electric shavers, drills, blenders, and others. The most used metallic matrices materials are copper, ferrous, and Niguel alloys. Compounds like MoS_2, WS_2, $MoSe_2$, NbS_2, $TaSe_2$, $MoTe_2$, h-BN, low melting metals like Ag, Sn and Pb, graphite and polytetrafluoroethylene (PTFE) are the most used as solid lubricants [11, 23–25]. The majority of the composites developed contain a high percentage of solid lubricant particles (15–40%) in order to obtain a low friction coefficient. This results in a largely discontinuous metallic matrix that exhibits poor mechanical properties.

The production of new high-performance self-lubricating composites containing second phase particles incorporated into a continuous matrix and having a low friction coefficient combined with high mechanical strength and wear resistance appears to be a promising solution for controlling friction and wear in energy efficient modern systems and points to an engineered microstructure.

3.2   Microstructural Model

The high mechanical and tribological performance is a consequence of the combination of matrix mechanical properties and structural parameters such as the degree of continuity of the metallic matrix, the shape, amount, and the size of solid lubricant particles and the resulting mean free path between them. In addition, it is clear that the development of high-quality composites demands improved mechanical resistance.

Figure 3.1 presents a schematic drawing of the ideal microstructure of a self-lubricating composite. The microstructure must consist of a continuous matrix containing regularly dispersed solid lubricant particles and take into account the mean free path between them and the active area to be covered by each one of them.

The solid lubricant dispersed in the volume of the composite material should be a completely discontinuous phase and many aspects such as the content of solid lubricant [26]; the size and size distribution of solid lubricant particles [27, 28] and the mean free path between the solid lubricant particles [29] have to be considered for microstructural optimization of the composite. To further minimize the interruption of the metallic matrix, the amount of the dispersed solid lubricant must be kept as low as possible. In this context, in addition to the traditional characteristics of the metallic matrix and of the solid lubricant powder particles such as type, amount, and shape, special attention must be paid to the relative size of particles (d_m/d_{sl}) since this parameter has a great influence on the degree of continuity of the matrix which, in turn, as already said, is determinant in the mechanical and tribological behavior of the composite. In fact, as illustrated in Fig. 3.1b, insoluble particles much smaller than those of the matrix tend to be located in the
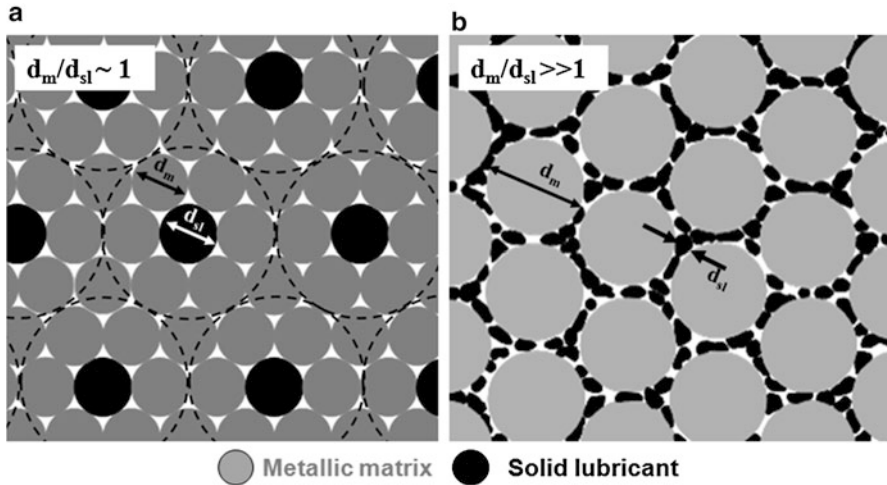
Fig. 3.1 Microstructural model (schematic). (**a**) Desirable distribution of the solid lubricant particles in the volume of the matrix and the corresponding area to be lubricated by each particle. (**b**) Continuity of the matrix

interstices occupying almost the entire interface between the metallic particles with a strong tendency to be the continuous phase which does not happen when they have equivalent sizes, Fig. 3.1a.

The metallic matrix which is the continuous phase that gives strength to the composite must be hard and tough enough to avoid the occurrence of micro-plastic deformation by friction and wear. The mass flow that occurs by plastic deformation may gradually cover the solid lubricant reservoirs and block the self-replenishment or resupply of solid lubricant to the interface. Further, it is important that the metallic matrix does not chemically react with the solid lubricant phase.

There are several possible manufacturing routes for producing such composites, in polymeric, metallic, or even ceramic matrices [30–32]. For the particle reinforced metallic matrix composites the methods to synthesize them are generally classified into (1) solid state processing, (2) liquid state processing, and (3) vapor deposition [33]. The most frequently used metallic matrix materials are copper [34], nickel [35], and ferrous alloys [36, 37]. Powder metallurgy techniques are especially suitable for the production of such composites.

3.3   Powder Metallurgy

For the development of metal-matrix composites, powder metallurgy (PM), widely used in industry, is a competitive and attractive technique because of its low cost when applied to large-volume production and because of its great versatility due to the suitability of the technique for tailoring the microstructure according to the

requirements imposed by a given application. In addition, PM processes are very advantageous for developing complex shape parts or even small-size components, which have been increasingly required due to the miniaturization of modern mechanical systems.

The high porosity of sintered components leads to reduced mechanical strength and load capacity when compared with fully dense materials. However, they have the potential to store lubricant that can be released during the use of the component [38, 39]. Also, the pores could eventually play an important role in the removal of wear debris from the sliding interfaces, as suggested by some authors [40]. Therefore, powder metallurgists are continuously searching for new alternatives and mechanisms to improve mechanical resistance and load support. In this sense, several processing parameters must be strictly controlled such as temperature and time of sintering, compression method, and techniques for the dispersion of the solid lubricant particles in the volume of the composite. Sintering is the most important step in the production of the composite. The variables in sintering are atmosphere, heating rate, temperature, dwelling time, and cooling rate. The sintering temperature should be lower than the decomposition temperature of solid lubricant. Reactions among the matrix, alloying elements and solid lubricant, which result in loss of solid lubricant, should also be avoided.

Special attention should be devoted to the compression technique. Several compaction techniques, like uniaxial die pressing, extruding, rolling, 3D prototyping, and powder injection molding, must be considered depending on the geometry and properties desired for the composite material. Uniaxial mechanical pressing, due to its low manufacturing costs, is still the most traditional processing route. It also produces the closest tolerances in the finished parts, thus nearly eliminating post-sintering operations such as machining [41]. However, depending on the configuration (single or double action), this technique presents gradients of porosity that may eventually be very high [42–44].

Recently [45], we presented a potential alternative for improving the mechanical strength of self-lubricating sintered composites: the use of the double pressing/ double sintering (DPDS) technique [46] originally developed by Hoeganaes [47] and used in the automotive industry. The goal of this method is to increase the density of composites by twofold pressing. According to German [48], reductions of 2–3% in porosity would result in up to a 20% increase in mechanical strength. Although more expensive, MIM has the advantage of flexibility of the processing parameters, which allows the production of very small parts presenting high geometric complexity, refined microstructure, and elevated final density [49]. That is not feasible with the current uniaxial die cold pressing process. For the case of self-lubricating composites, the metal injection molding method is particularly indicated due to the small powder size which induces more homogeneous tribolayers covering the whole interface, Fig. 3.1a.

Roughly speaking, in MIM process, metal powders are premixed with polymeric binders. The mixture is heated and forced under pressure into a die cavity, where it cools and is subsequently ejected. The polymer is then removed (debinding stage) and the component sintered to the required density, Fig. 3.2.
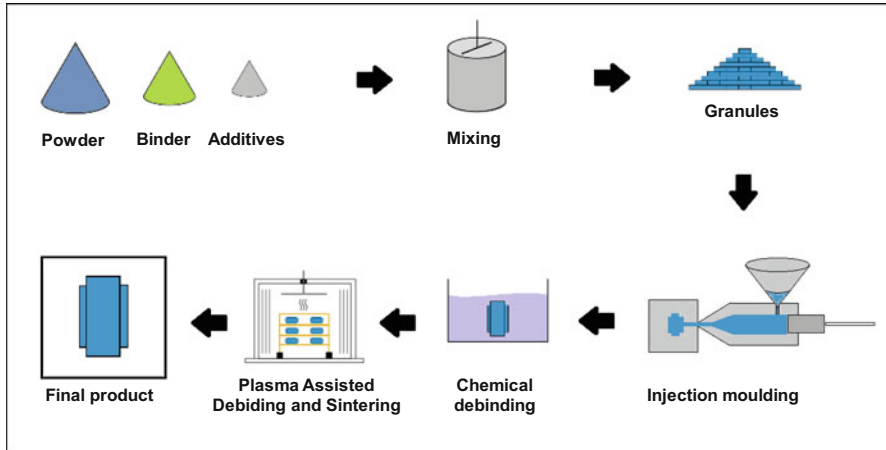
Fig. 3.2 Metal injection mold processing route

The debinding stage, during which polymer is removed, can greatly influence the mechanical properties of the sintered component [49, 50]. In our case, the debinding was carried out in a stepwise process: chemical debinding was followed by plasma-assisted thermal debinding. The chemical step consisted of the dissolution in hexane of the low molecular weight components of the binder system, forming an open pore network within the injected parts.

The thermal debinding, as well as the sintering, was performed in a single thermal cycle (plasma-assisted debinding and sintering – PADS) [50]. In summary, its advantages are short processing time (debinding and sintering in about 10 h versus 90 h for the thermochemical classical processes) and no binder residues after debinding. This process allows sintering in a single cycle and eliminates a cleaning procedure after every cycle. In the plasma-assisted debinding process, the polymer macromolecules are dissociated by bombardment of energetic electrons (inelastic collision) resulting in hydrocarbon radicals (C_xH_y) whose recombination is prevented by the presence of atomic hydrogen present in the hydrogen plasma, Fig. 3.3b. The reaction of atomic hydrogen with hydrocarbon radicals results in hydrocarbon gas that is removed from the reactor chamber via the vacuum pump.

The plasma reactor, developed in [51], was specially designed for the PADS process and described in [50–52] allows the control of the processing temperatures and the heating rates independently of the plasma parameters. The vacuum chamber, shown schematically in Fig. 3.3a, contains electrodes for the generation of plasma DC and electrical heaters for heating control. The samples were set on ceramic plates supported by the structure of the anode and were initially processed in floating potential plasma. Abnormal hydrogen glow discharge was then generated and the power supply voltage was biased to the cathode during the isothermal sintering.

As already pointed out (Fig. 3.1a), the ideal microstructure of a self-lubricating composite must consist of a continuous matrix containing regularly dispersed solid
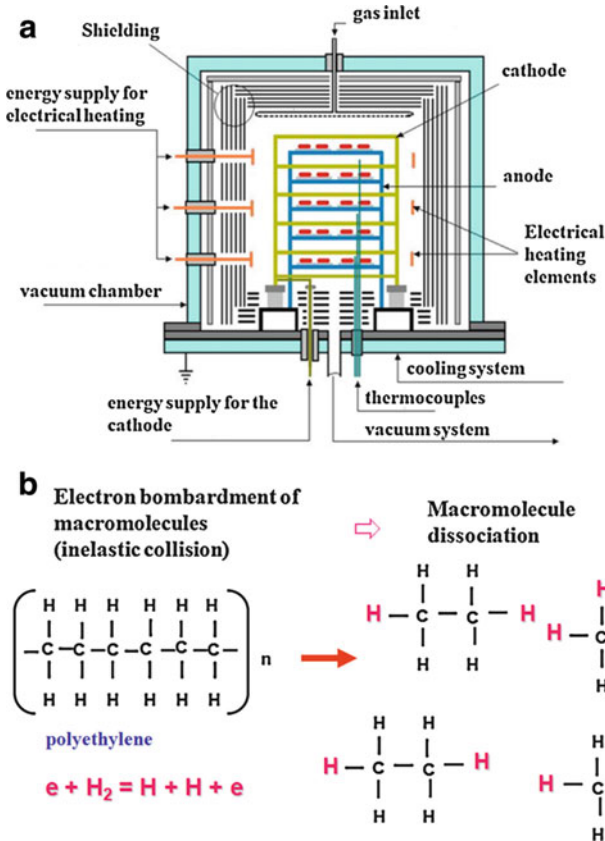
Fig. 3.3 Plasma-assisted debinding and sintering process. (**a**) Hybrid reactor [50]. (**b**) Macromolecule dissociation principle

lubricant particles. Unfortunately, such an ideal distribution of the solid lubricant particles is not obtained simply by blending metallic and solid lubricant powders.

In order to produce a self-lubricating sintered composite, there are basically two ways of dispersing the solid lubricant particles in the volume of the metal matrix [53, 54]:

 (i) Mixing the solid lubricant particles with matrix powders
(ii) "In situ" generation of the solid lubricant particles during the sintering by dissociation of a precursor mixed to the powders of the metallic matrix

In the first method, where the composite is obtained by mixing the metallic matrix powders with the solid lubricant particles, the shear stresses that occur during mixing and compacting spread the solid lubricant by shearing between the powder particles of the metal matrix. This leads to an undesirable arrangement in which the solid lubricant covers the metallic particles to a large extent [55]. The presence of these
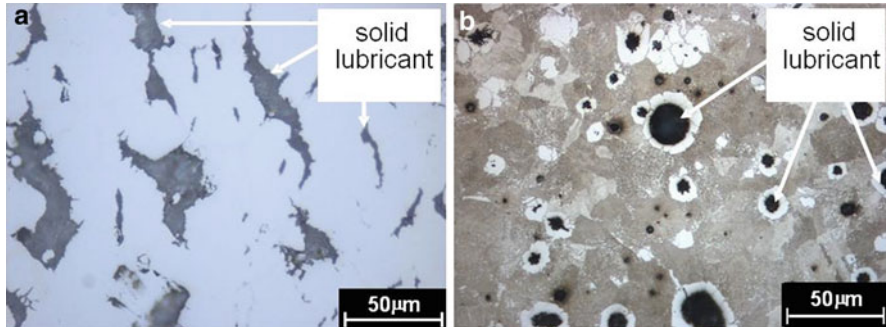
Fig. 3.4 Solid lubricant particles dispersion. (**a**) Mixing of powders prior to compaction. (**b**) In situ generated by decomposition of a precursor

layers of insoluble solid lubricant hampers the formation of contacts between the particles during sintering. This results in a metallic matrix with a high degree of discontinuity, Fig. 3.4a, and leads to a composite material with reduced mechanical strength.

There are two possibilities to overcome these difficulties. The first one is to rearrange the solid lubricant phase in discrete agglomerates by the capillary action of a liquid phase. The liquid phase spreads and penetrates the interfaces between the metal and the lubricant, thus pushing the solid lubricant and rearranging it in agglomerates. The second one is to produce the solid lubricant phase in situ during sintering by decomposition or dissociation of a precursor, giving rise to a more continuous and sound matrix, Fig. 3.4b.

Preliminary studies evidenced that the in situ generation of the solid lubricant phase particles during the sintering by the dissociation of a precursor was the most promising production route.

3.4 In Situ Generated Graphite

Silicon carbide (SiC), molybdenum carbide (Mo_2C), chromium carbide (Cr_3C_2), etc., are potential precursors to generate graphite nodules in ferrous matrix [56, 57]. Among them, those inducing the stabilization of the body-centered cubic phase of iron (α-Fe) are the most indicated in order to produce iron-based self-lubricating composites. SiC is particularly appropriate since it features a high carbon content, and silicon is a strong alpha phase stabilizer in addition to being one of the most effective hardening elements of ferrite [58].

Figure 3.5 shows typical aspects of the microstructure of the composites.

The reference alloy (Fe + 0.6 C + 4 Ni) presented a microstructure constituted of perlite (P) + ferrite (α), Fig. 3.5a, whereas the addition of SiC to the feedstock powder induced the formation of graphite nodules. The graphite nodules (G) are always surrounded by ferrite (α) rings, Fig. 3.5b.
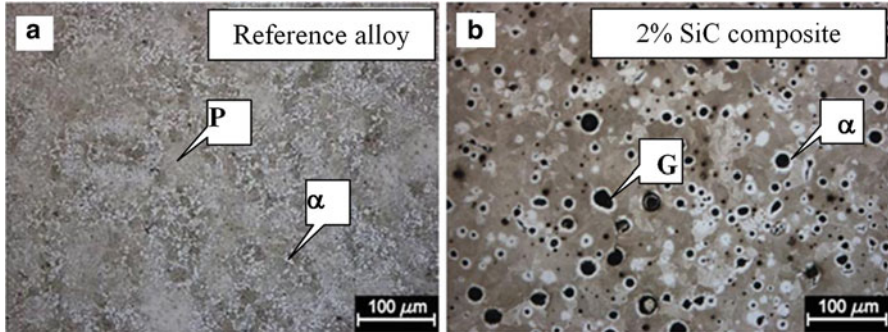
Fig. 3.5 Typical aspects of the microstructure. (**a**) Reference alloy (matrix alloy – Fe-0.6%C-4% Ni). (**b**) 2 wt% SiC composite. Sintering temperature 1150 °C

The evolution of the microstructure depends on precursor (SiC) content, sintering parameters (temperature, time, and atmosphere), and the previous composition (other alloying elements) of the ferrous matrix. [53]. For example, the presence of carbon in the matrix prior to the startup of SiC dissociation reduces the dissolution of the carbon originated from the dissociation of SiC and increases the size and the amount of the graphite nodules formed [36, 59]. The presence of Ni, a strong stabilizer of the face-centered cubic phase of iron (γ-phase) of the iron matrix, positively influences the morphology of the graphite nodules [36].

Such microstructure formation was expected from thermodynamic considerations as evidenced by the Ellingham diagram presented in Fig. 3.6a and its evolution depends on sintering time and temperature, as well as on the amount of SiC added to the ferrous matrix. This is well described in a recent paper [53].

Roughly, during the sintering, at the initial stage of the dissociation of the SiC particles, silicon and carbon atoms diffused into the ferrous matrix, Fig. 3.6b. However, the continuous enrichment of the ferrous matrix with Si around the former silicon carbide particles leads to stabilization of the body-centered cubic structure of the ferrous matrix (ferrite) in which the solubility for the carbon atoms is very low (solubility ≤0,022 wt%), [60], drastically reducing the dissolution of graphite. The dissolution of silicon, in contrast, is maintained [60]. As a consequence ferrite rings are formed around the former SiC particles, Fig. 3.7a [53, 54, 61].

The remaining carbon forms graphite nodules (size ≤20 μm), Fig. 3.7b which present a nanostructured stacking of graphite layers a few tenths of nanometers thick, Fig. 3.7c, d. The evolution of such microstructure depended on the amount of SiC, as well as on sintering temperature and time and is fully described in a recent paper [59]. The precipitation of graphite nodules started at temperatures higher than 1100 °C. At this temperature the precipitation is important for times superior to 1 h as evidenced by XRD analysis [61].

Finally, Fig. 3.8 presents line profiles of C and Si throughout a graphite nodule and a ferrite ring evidencing the low solubility of carbon in the ferrite and the depletion of silicon in the former SiC particle.

Fig. 3.6 Thermodynamic equilibrium. (**a**) Ellingham diagram. (**b**) Initial stage of SiC dissociation, SEM
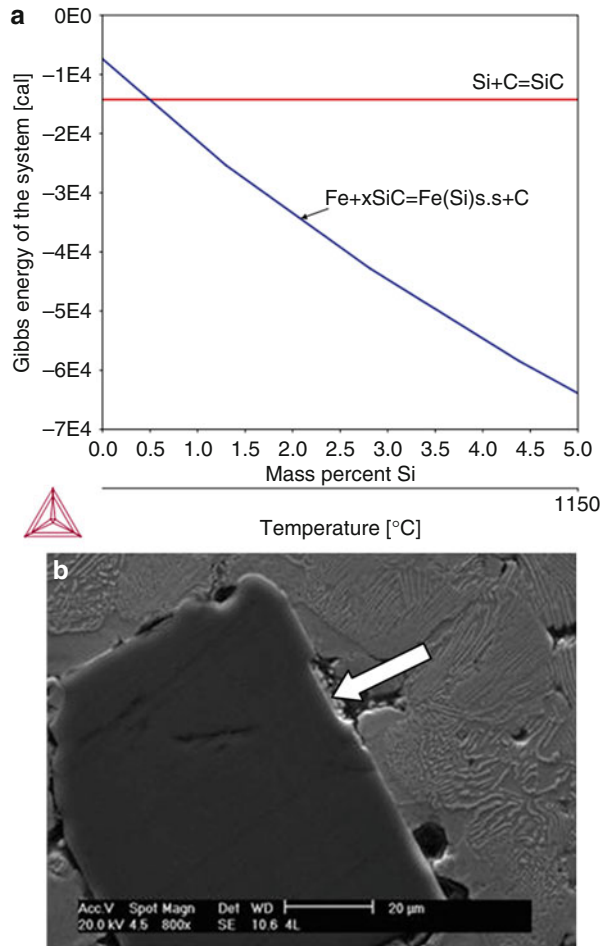
The nodules are composed mostly of carbon, whereas the ferrite ring around the nodule has an almost constant high concentration of silicon, and the carbon concentration is greatly reduced. Outside the ferrite ring, the silicon concentration decreases, and the carbon concentration in the matrix increases. This interface is the separation between the ferritic (α-Fe) phase and pearlitic (γ-Fe) regions, thus confirming the formation of the carbon nodules by the SiC dissociation and the formation of a diffusion barrier due to α-Fe phase stabilization by silicon.

3.5   Tribological Characterization

The tribological behavior was evaluated using two types of experiments schematized in Fig. 3.9:
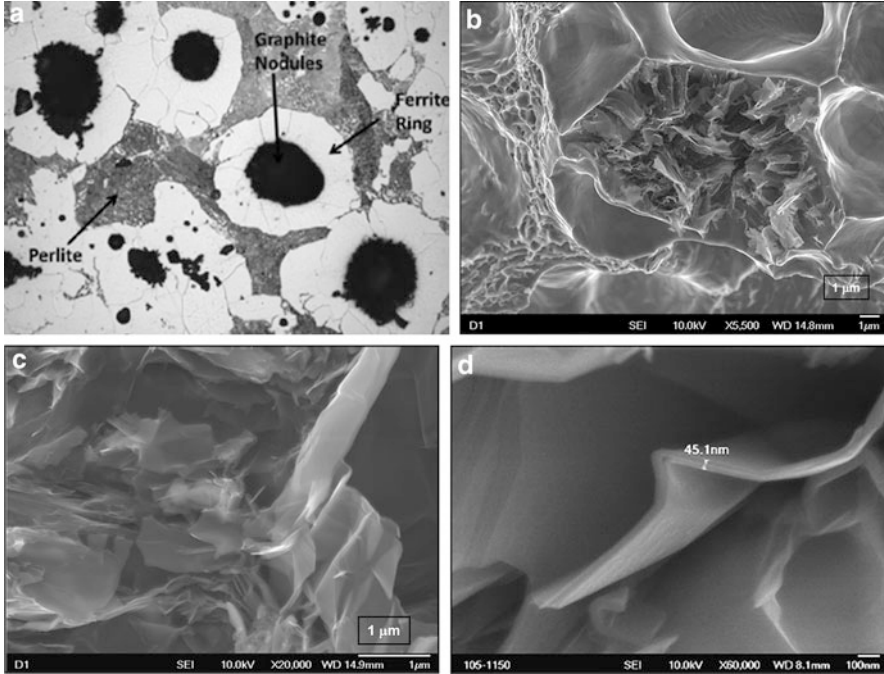
Fig. 3.7 Typical aspects of the microstructure. Composite Fe-0.6C-4 Ni-2 SiC. (**a**) Ferrite ring. (**b**–**c**) Graphite nodule (fractography). (**d**) Graphite layer

(a) Reciprocating sliding tests were conducted at constant normal load to access the friction coefficient and wear rates of specimens and counter-bodies.

(b) Reciprocating sliding tests were carried out in an incremental loading mode. In this case, by increasing the normal load in increments of 7 N at 10 min. intervals, the scuffing resistance was determined. The scuffing resistance was defined as the work (N m) at which the value of the friction coefficient first rose above 0.20 (lubricity effect) [12].

In both kind of experiments, a hard steel AISI 52100 ball (diameter 5 or 10 mm) was fixed on a pivoted arm and rested against the specimen surface under constant stroke (5 mm) and frequency (2 Hz). The tests were conducted under controlled relative humidity (50%) and temperature ($22 \pm 4\,°C$).

Wear scars were analyzed by using SEM-EDX as well as FEG-SEM, micro-Raman spectroscopy, Auger electron spectroscopy, and laser interferometry.

3.6 Mechanical Properties

The evolution of the mechanical properties with precursor content and sintering temperature is illustrated in Fig. 3.10.
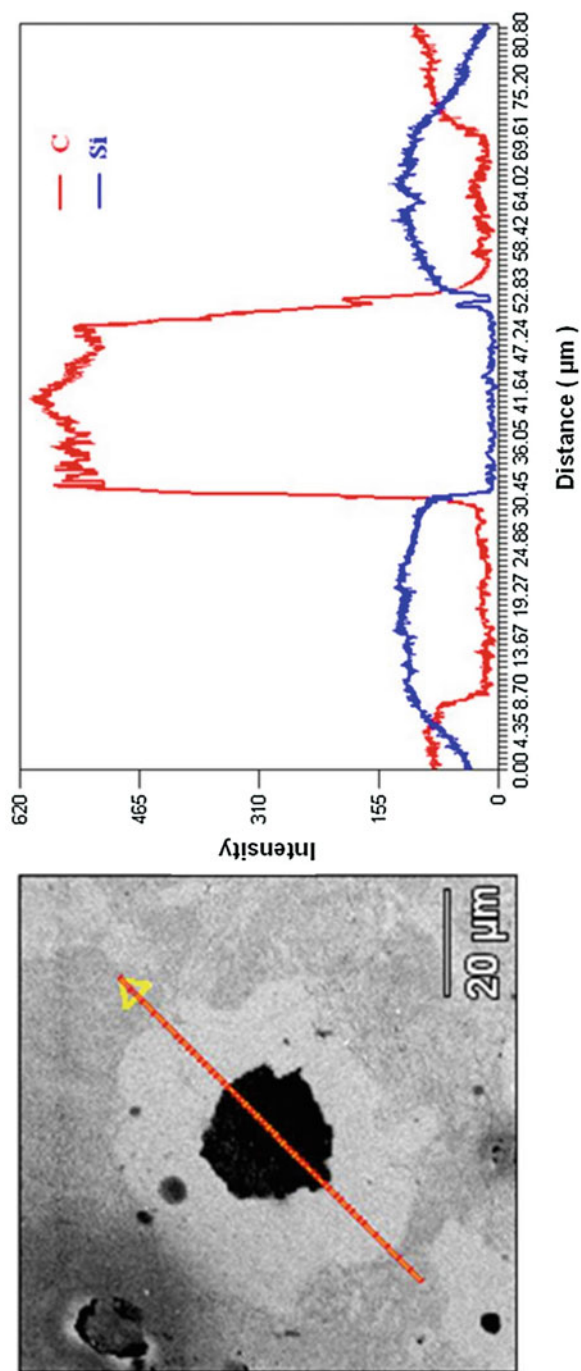
Fig. 3.8 Line profile showing the concentration of silicon and carbon along the graphite nodule and the surrounding metal matrix
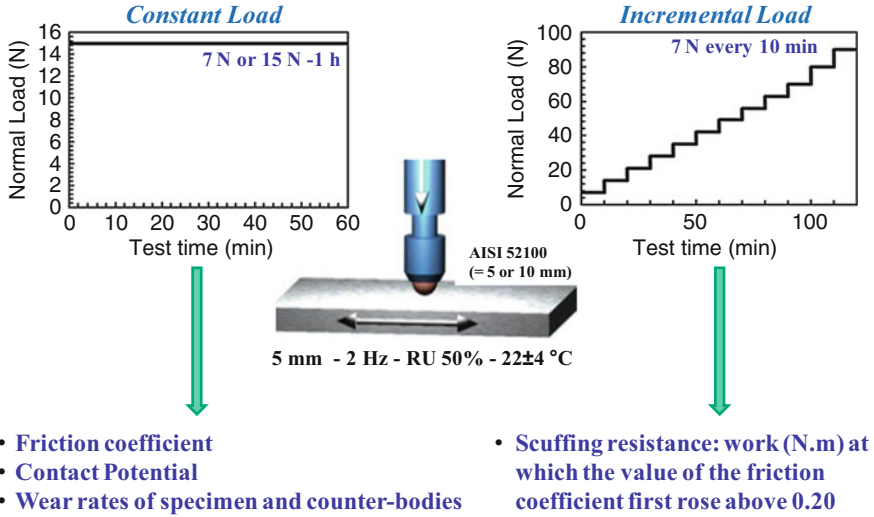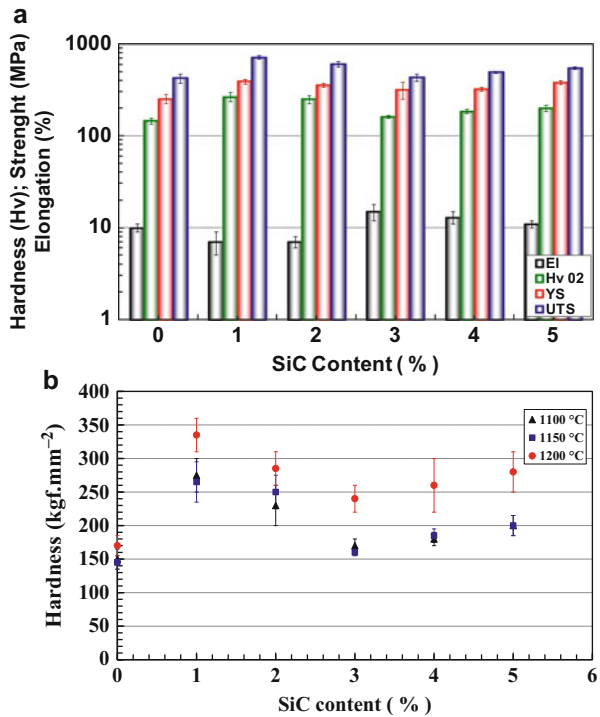
Fig. 3.9 Tribological characterization

Fig. 3.10 Typical evolution of the mechanical properties. (**a**) Effect of SiC content on mechanical properties for composites sintered 1150 °C. (**b**) Influence of SiC content and sintering temperature on hardness
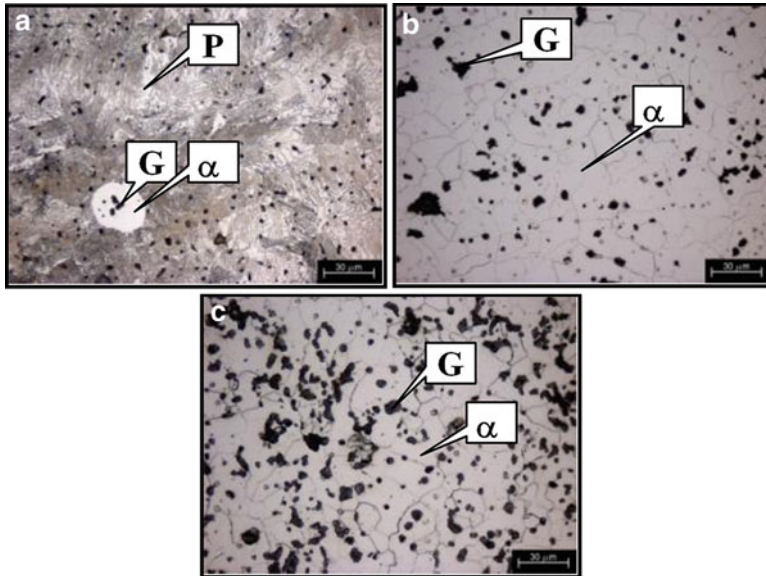
Fig. 3.11 Typical microstructures. Sintering temperature 1150 °C. (**a**) 1% SiC; (**b**) 3% SiC; (**c**) 5% SiC

The addition of SiC induced a quite complex evolution of the mechanical properties, Fig. 3.10a. There is a sharp increase up to a maximum for additions of 1% SiC. Then the hardness decreased to a minimum at 3% SiC and afterwards gradually increased. The strength of the composites follows the same behavior whereas, of course, the elongation behaved in the opposite sense.

In terms of hardness, Fig. 3.10b, the dissociation of SiC particles produced harder composites than those of the metallic matrix alone. There is a sharp increase up to a maximum for additions of 1% SiC. Then the hardness decreased to a minimum at 3% SiC and afterwards gradually increased. Indeed, for composites presenting 3% SiC the metallic matrix is mainly constituted of ferrite (α), Fig. 3.11b, whereas for smaller SiC contents the microstructure presents a certain amount of perlite (P), Fig. 3.11a. For higher SiC amounts, Fig. 3.11c, it is reasonable to suppose that the great availability of silicon induces a larger hardening of the matrix (ferrite).

The mechanical properties of the composites are a compromise between the two different effects of the dissolution of the SiC particles [53, 61]:

 (i) An increase in the mechanical resistance caused by the strengthening of the metallic matrix due to the dissolution of Si
(ii) A decrease in the mechanical resistance as a consequence of the formation of graphite nodules during the sintering process, which decreases the degree of continuity of the metallic matrix.

Silicon is known to be one of the most efficient promoters of the hardening of ferrous matrix by the formation of substitutional solid solution [62, 63].

On the other hand, the sintering temperature produced a strong effect on the mechanical properties as illustrated by hardness, Fig. 3.10b. The high sintering temperature produced harder (up to 50%) composites whereas the variation from 1100 °C to 1150 °C produced almost no effect. The higher values presented by the samples sintered at 1200 °C are supposed to be mainly due to the higher degree of the homogeneity of the composites (in particular the distribution of Si and pearlitic regions in the matrix) sintered in this higher temperature. However, for composites with 4% and 5% SiC sintered at 1200 °C, values of yield and tensile stress decrease, which was related to the formation or "line structures" reducing matrix continuity and affecting the material properties [59].

3.7 Tribological Behavior

3.7.1 Introduction

In this section, the tribological behavior of self-lubricating composites produced taking advantage of the powder injection molding process, the recently introduced plasma-assisted debinding and sintering (PADS) process, and the in situ formation solid lubricant particles is presented and discussed. In this case, we obtained the in situ formation of graphite nodules in the volume of the sintered composites during sintering simply by dissociation of particles of silicon carbide (SiC) mixed to the metallic matrix powders prior to the compaction.

Recent studies concluded that a transfer film is found on the sliding surfaces [53]. The formation of such a film on the sliding interfaces seems to be the key for achieving low friction and long wear life in most solid-lubricated surfaces [13]. It was found that, initially, transfer films were not present but were formed as a result of surface wear and subsurface deformation. These films are continuously replenished by embedded graphite particles dispersed in the matrix [64].

The effects of precursor content (0 to 5 wt% SiC) and of sintering temperature (1100 °C, 1150 °C and 1200 °C) on tribolayer durability, average friction coefficient in the lubricious regime ($\mu < 0.2$), and wear rate of the specimens and counter-bodies are presented and discussed. In addition, the effect of the metallic matrix composition (Fe-C; Fe-C-Ni; Fe-C-Ni-Mo) and surface finishing are also presented. Special emphasis is given to the protective tribolayer.

3.7.2 Materials

Sintered composites with different chemical compositions were produced by mixing carbonyl iron powder (Carbonyl BASF grade OM) with elemental powder of the alloying elements. The carbonyl iron used had a particle size of 7.8 μm and

contained 0.8% carbon. Different contents of silicon carbide (Cobral) powder (1%, 2%, 3%, 4%, and 5% SiC) having particle size of 10 μm were added to the carbonyl iron powder. The feedstock for injection was prepared in a Haake Sigma mixer (180 °C, 70 rpm, 90 min) using 8% of an organic binder system containing paraffin wax, polypropylene, stearic acid (surfactant), ethylene vinyl acetate copolymer (EVA), and amide wax.

Samples with the appropriate geometry for performing tensile and tribological tests were injected (injection pressure of 100 MPa) using an Arbourg 320S injection molding machine. The debinding was performed in two steps: a chemical debinding followed by plasma-assisted thermal debinding. The thermal debinding, as well as the sintering, was performed in a single thermal cycle in a plasma reactor, i.e., using the plasma-assisted debinding and sintering (PADS).

A hydrogen abnormal glow discharge was generated at a pressure of 133 Pa (1 Torr) and the gas flow was adjusted to $3.33.10^{-6}$ m^3 s^{-1} (200 sccm). The power supply voltage biased to the cathode was fixed at 500 V. A heating rate of 0.7 °C/min was fixed up to 500 °C for the plasma-assisted thermal debinding step. Then, the heating rate was increased to 5 °C/min up to the sintering temperature. The isothermal sintering was processed at 1100 °C, 1150 °C, and 1200 °C for 60 min.

In order to analyze the effect of the metallic matrix, three compositions of sintered composites (Fe–Si–C, Fe–Si–C–Ni, and Fe–Si–C–Ni–Mo) were also produced. The same iron powder was used (Carbonyl BASF grade OM). The alloying elements Ni and Mo were mixed to the feedstock in the form of elemental Ni (Vale Inco Type 123) and elemental Mo (H.C. Starck Type) powder. Silicon was added in the form of 3 wt% silicon carbide powder (Cobral) aiming at its dissociation during sintering. The same processing route was used but just one sintering temperature and time (Ts = 1150 °C- 60 min) were used.

3.7.3   Tribological Evaluation

3.7.3.1 Incremental Load Tests (Scuffing Resistance)

Typical results are shown in Fig. 3.12.

All results present similar behavior. There is a transient associated with the onset of contact between specimen and counter-body at the beginning of tests before a high lubricity steady state is reached. The reasons for the difference in the evolution of the friction coefficient within the transient period are not yet well understood and will not be treated in the present chapter. However, it is reasonable to suppose that the stabilization of the friction coefficient is related to the generation of a protective tribolayer, where the transient corresponds to the kinetics of formation of the layer. As long as the formation rate of the tribolayer is different from the degradation rate, friction coefficient will vary. Once this formation rate is equal to or greater than the degradation rate, a steady state is reached.

All specimens behaved in a similar manner in the lubricious regime. However, low SiC content composites (e.g., 1% SiC) presented higher friction coefficient which gradually increases with the sliding distance associated with a shorter and
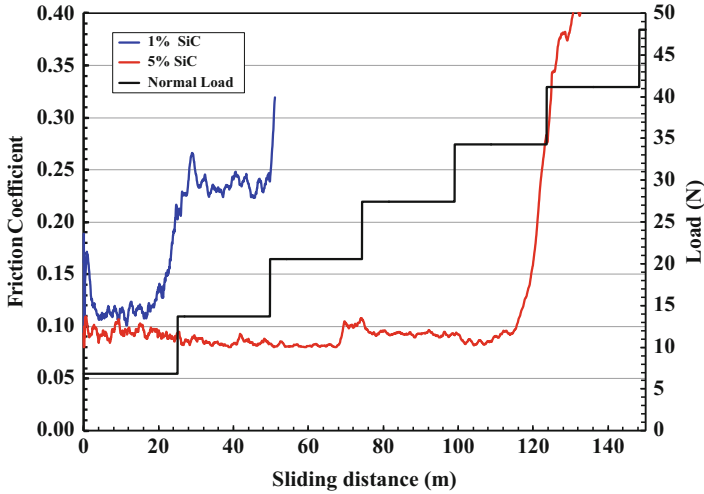
Fig. 3.12 Typical evolution of friction coefficient with sliding distance and applied normal load
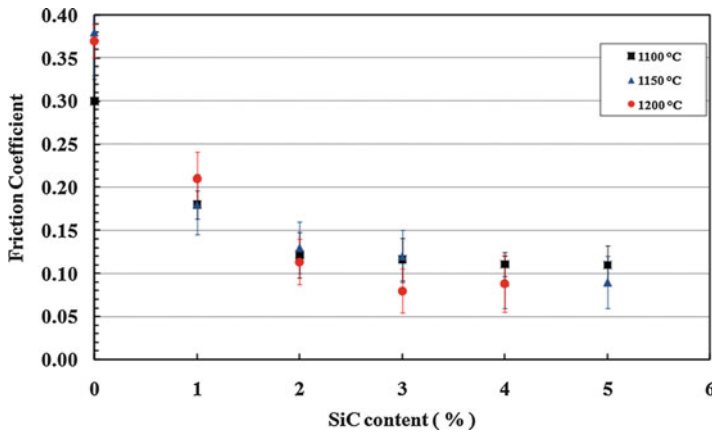

Fig. 3.13 Effect of SiC content and of sintering temperature on the average friction coefficient during the lubricious regime

almost equivalent scuffing resistance, whereas the high SiC content (e.g., 5% SiC) composites exhibited lower friction coefficients coupled with much longer period in the lubricious regime signalized by a rapid increase in the friction coefficient. The friction coefficient values for each test were computed by averaging the lubricious steady-state values.

The influence of the precursor content and of the sintering temperature on the friction coefficient behavior is synthesized in Fig. 3.13.

Independently of the sintering temperature, increasing the precursor content and, as a consequence, the number of graphite nodules produced a reduction of the

average friction coefficient. In general, the reduction was substantial, up to 3% SiC. For higher values of SiC content, the friction coefficient was almost constant. It is reasonable to suppose that graphite foils are removed from the in situ generated graphite nodules and remain at the interface thus contributing to the formation of a protective tribolayer. Due to the small size of the powders, the mean free path between graphite nodules is also small and the complete "coverage" of the surface between nodules is easily reached. As a consequence, the number of graphite foils generated in composites containing more than 3% of SiC is sufficient to produce the protective layer and low friction coefficients. Additionally, there is almost no effect of the sintering temperature on the average friction coefficient.

A comparison between Figs. 3.10 and 3.13 shows that there is, definitely, no correlation associating the friction coefficient with mechanical properties of the composites.

Figure 3.14 presents typical aspects of the wear scars. The test was interrupted at the normal load of 14 N which is within the lubricious regime ($\mu < 0.2$).

At low magnifications, Fig. 3.14a, the wear scar appears quite homogeneous. It presents flat and smooth regions where contact with the counter-body occurred. It seems that there is a protective layer on the active interface (brown/gray areas, confirmed, by using back scattered electrons, to be composed of elements presenting low atomic number). It is reasonable to suppose that graphite foils are removed from the in situ generated graphite nodules and remain at the interface (Fig. 3.14b) thus contributing to the formation of the protective tribolayer. Due to the small size of the powders, the mean free path between graphite nodules is also small and the complete "coverage" of the surface between nodules is easily reached. As a consequence, the number of graphite foils generated in composites containing more than 3% of SiC is sufficient to produce the protective layer and low friction coefficients thus explaining the saturation of the friction coefficient variation with precursor content, Fig. 3.13.

On the other hand, since the tribolayers also degrade under the action of the sliding (Fig. 3.14c).

Figure 3.14d presents a typical Raman spectra obtained in the central region of the wear scar. It clearly presents a widened G band (associated with the sp^2 hybridization) and a D band (associated with crystallinity disorder). The widening of the bands, the ID/IG ratio, and the size of the graphite crystallites are, accordingly to literature [61, 65–68], clear evidence of disorder in the material. They are also a strong indication of the presence of the so-called turbostratic 2D graphite which presents longer interlamellae distances among the graphene foils when compared to the highly oriented 3D graphite coupled with a strong misalignment of the graphene foils. Moreover, the analysis of the second-order band G′ confirms the greater contribution of the 2D graphite to the formation of the D band.

The increase in distance may induce low interaction between these atomic planes and is, probably, the origin of the low friction coefficient [69].

To further understand this point, a few other types of graphite were analyzed under the same tribological configuration: They are graphite nodules in a nodular cast iron, and the contact was submerged in graphite in powder. The matrix alloy (graphite-free – Fe 0.6 wt% C) was also tested as a reference.
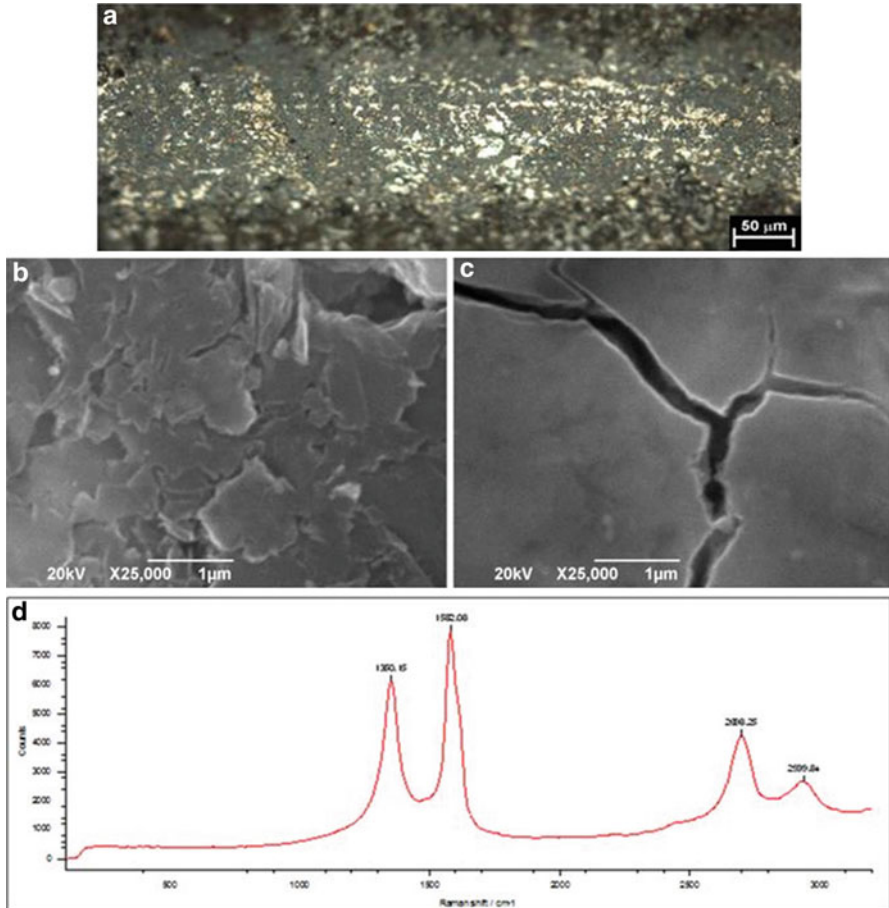
Fig. 3.14 Typical wear scars produced in the lubricious regime ($\mu < 0.2$). Fe + 0.6C + 5SiC. (**a**) General aspect, optical microscopy; (**b**, **c**) FEG-SEM; (**d**) Raman spectra

Figure 3.15 shows the average friction coefficient (steady state) of different materials.

The reference alloy presented the highest friction coefficient. The presence of graphite (nodules in nodular cast iron and graphite in powder) strongly reduced the friction coefficient (170% and 290%, respectively). The addition of 3 wt% SiC further reduced the friction coefficient (530%) and induced a remarkably low value (0.06).

Figure 3.16 presents the typical Raman spectra of different graphite types.

They clearly show a G band at approximately 1580 cm^{-1}. The spectrum of the graphite nodules produced by the SiC decomposition (Fig. 3.16a) clearly presents a D and a D$'$ band both associated with crystallinity disorder. The analysis of the spectra shows many evidence (the widening of the bands, the I_D/I_G ratio, the size of
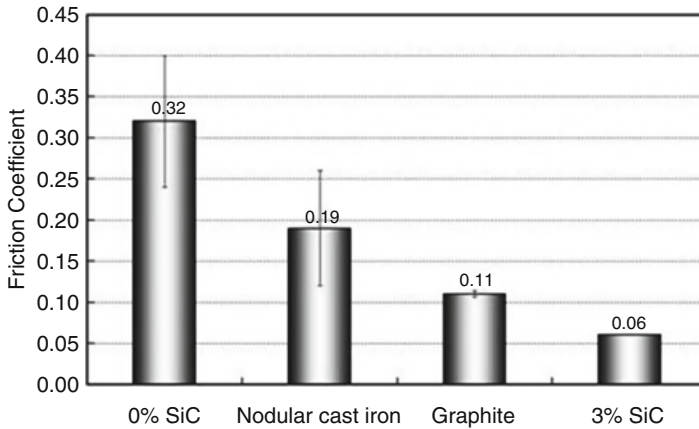
Fig. 3.15 Effect of graphite type on friction coefficient

the graphite crystallites, and the shape of the second-order G′ band) of the presence of the so called turbostatic graphite (2D graphite). Moreover, the analysis of the second-order G′ band (very sensitive to the stacking order of the graphene sheets along the c axis [70, 71]) confirms the greater contribution of 2D graphite to the formation of the D band. Graphite associated with graphite powders, Fig. 3.16b, and nodular cast iron, Fig. 3.16c, is characterized as 3D graphite and is highly aligned according to the literature [65–67].

According to the literature [61–68, 72], the widening of the bands, the ID/IG ratio (widely used for characterizing the defect quantity in graphitic materials) [70–73] and the size of the graphite crystallites (La) are clear evidence of disorder in the graphite nodules in the composite Fe-0.6 wt% C + 3 wt% SiC. They also strongly indicate the presence of the so-called turbostatic 2D graphite, which has highly misaligned graphene planes separated by larges paces. A recent paper presents the main aspects of the 2D turbostatic graphite including a comprehensive analysis of the Raman spectra of the different graphite types [72] clearly evidencing that major contribution to the G′ band stems from graphite 2D, not from 3D graphite.

Transmission electron microscopy, Fig. 3.17, confirmed the large interplanar distance, Fig. 3.17b ($\geq$3.499 Å against 3354 Å for the high aligned 3D graphite), among the graphene foils and the misorientation of the graphene foils, inset in Fig. 3.17c.

Figure 3.17a, b show bright field images of graphite sheets obtained from the graphite nodules of a Fe +0.6C + 3SiC composite and the corresponding SAED. Figure 3.17c presents high-resolution (HRTEM) image with fringes representing individual carbon layers and the SAED pattern (inset) taken from this region. Moreover, the increased interlayer spacing could be correlated to the stacking fault disorder, inherent of turbostatic graphite [74, 75].

These large spaces associated with the misalignment among the graphene planes drastically decreased the interaction among the planes, which results in a low shear
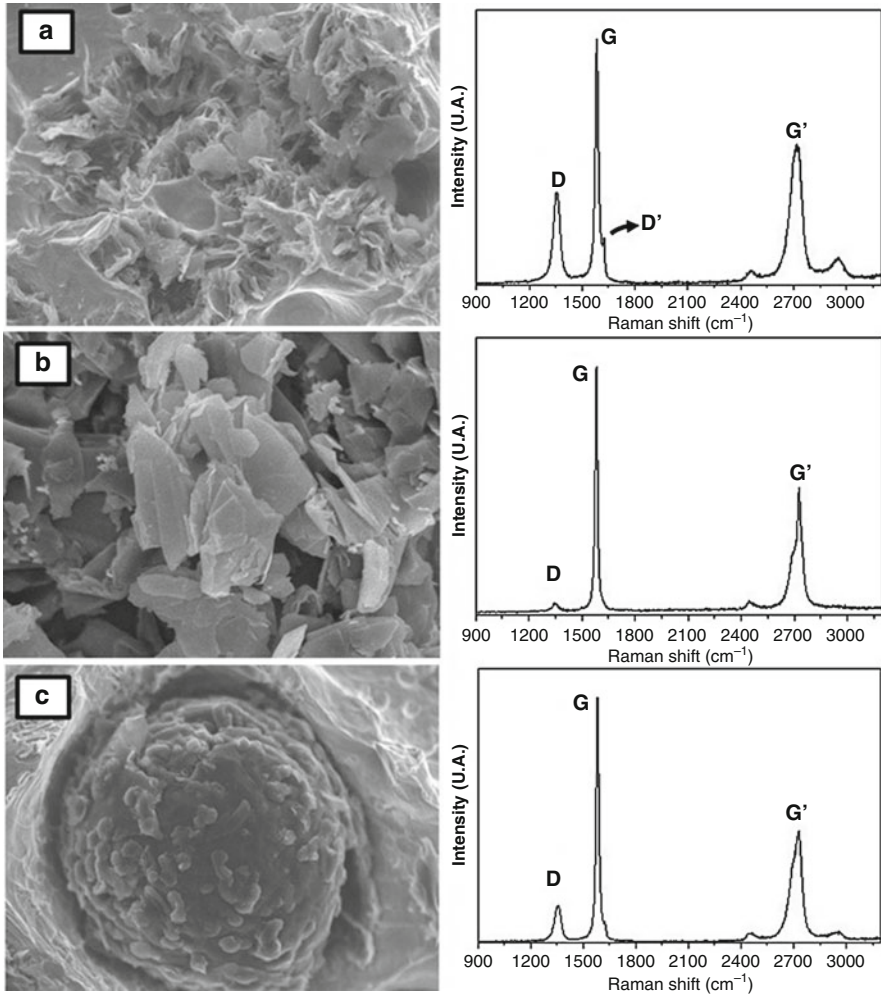
Fig. 3.16 Typical Raman spectra. (**a**) Graphite nodule obtained via SiC dissociation, (**b**) graphite in powder, (**c**) graphite nodule in nodular cast iron [72]

strength. Thus, it is reasonable to suppose that during the reciprocating sliding, the graphite planes easily shear and maintain a constantly lubricated contact interface.

There is almost no effect of the sintering temperature on the lubricious average friction coefficient. On the contrary, the sintering temperature strongly influences scuffing resistance, Fig. 3.18. The low sintering temperature induces significantly higher scuffing resistance (5×).

For the extreme sintering temperatures, increasing SiC content up to 2% induced a strong increase in scuffing resistance and then it remained almost constant, Fig. 3.18. In this case, the saturation effect is reached at 2% of SiC indicating that the self-replenishment provided by the graphite nodules is already active at this
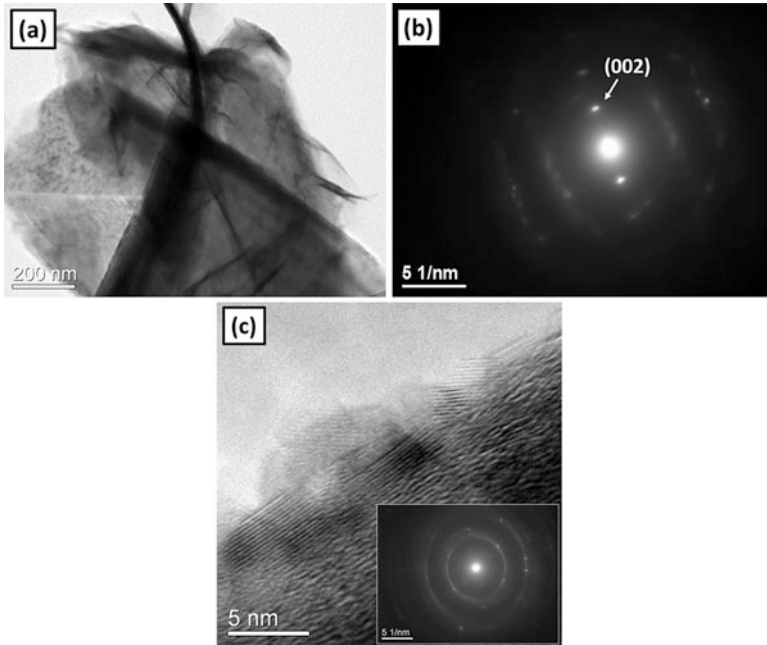
Fig. 3.17 (**a**) Bright field TEM micrograph, (**b**) the corresponding SAED pattern, and (**c**) high-resolution TEM image of graphite sheets obtained from graphite nodules for a Fe + 0.6C + 3SiC sample. The inset in (**c**) shows a typical SAED pattern recorded from this region (graphite sheets) [72]
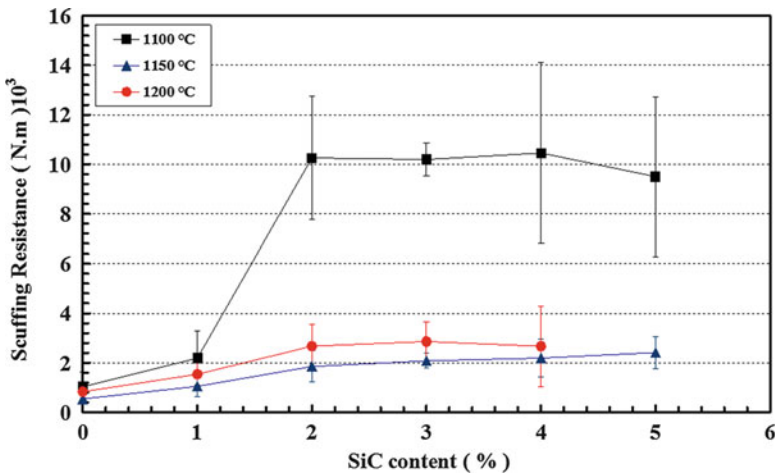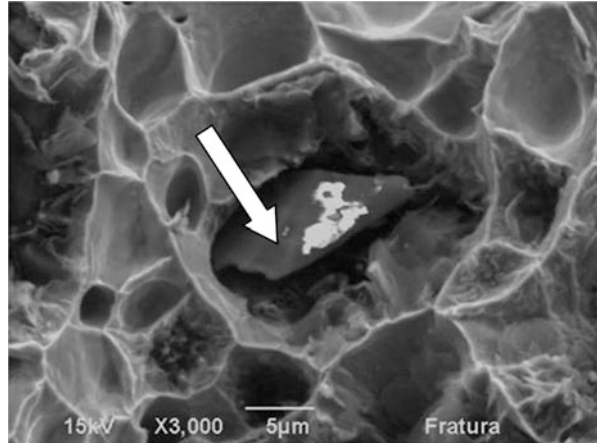

Fig. 3.18 Effect of SiC content and of sintering temperature on scuffing resistance

Fig. 3.19 Typical undissociated SiC particle. Fe + 0.6C + 3SiC, 1100 °C, 60 min

lower value. However, for the intermediate sintering temperature there is an almost monotonous increase of scuffing resistance after this threshold is reached.

Again, there is definitely no correlation associating the scuffing resistance with mechanical properties of the composites. In order to further understand why the low sintering temperature induced higher scuffing resistance, Fig. 3.18, the samples sintered at 1100 °C were cryogenically fractured and then the surfaces were analyzed using SEM. A typical aspect of the graphite nodules present in Fe + 0.6C + 3SiC composite is illustrated in Fig. 3.19.

The white arrow points to a partially dissolved SiC particle. EDS point analysis showed that there is, probably, a ring of ferrite around the nodule since the chemical composition was higher than 2.1 wt% Si.

Taking into account that the metallic matrix is continuous, it is reasonable to suppose that the solid lubricant, or its precursor, does not contribute to the mechanical resistance of the composite as already illustrated and discussed in the hardness/SiC content relationship. However, the presence of undissociated particles of SiC may produce a greater load-bearing capacity and the protection of the matrix/tribolayer, thus inducing higher scuffing resistance.

3.7.3.2 Constant Load Tests

Effect of Precursor Content and Sintering Temperature
In this section, the effect of the sintering temperature (1100 °C, 1150 °C, and 1200 °C) and SiC content (0–5 wt%) on the tribological behavior (friction coefficients and wear rates of specimens and counter bodies) is presented and discussed.

In all cases, the evolution of the friction coefficient with time exhibited a transient state at the beginning of the tests; then, a steady state with similar fluctuations from the start to the end of the test was attained, Fig. 3.30. The evolution of the average steady-state fiction coefficient with precursor content and sintering temperature is presented in Fig. 3.20.
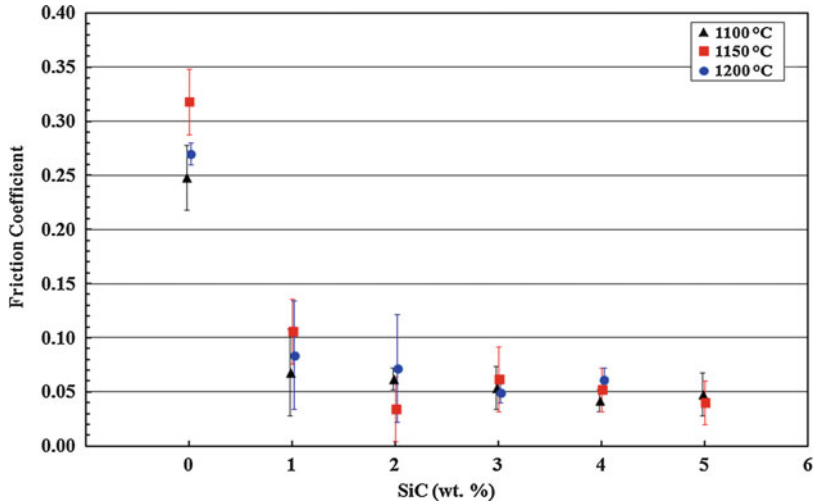
Fig. 3.20 Effect of the silicon carbide content and sintering temperature on the steady-state friction coefficient. *The x values were slightly shifted (±0.02) to the left and to the right in order to separate overlapping symbols*

Independently of the sintering temperature, an increase of the precursor content, which increased the number of 2D turbostratic graphite nodules, reduced the average friction coefficient. In general, the reduction was substantial (up to 3 wt% SiC).

For higher SiC contents, the friction coefficient was almost constant. It is also noticeable that the friction coefficient was hardly affected by the sintering temperature. All composites showed a considerably smaller friction coefficient (one order of magnitude) than the matrix alloys (carbide-free alloys). Again, there is, definitely, no correlation associating the friction coefficient with the mechanical properties of the composites and the outstanding tribological behavior may be attributed to the presence of the so-called turbostratic 2D graphite.

Figure 3.21a shows the effect of the silicon carbide content and sintering temperature on the wear rate of the specimens.

The addition of SiC, which creates 2D turbostratic graphite nodules, clearly enhances the tribological behavior. The matrix alloy showed a considerably higher (one order of magnitude higher) wear rate than the composites. When the SiC content increased, there was a decrease to a minimum at 3 wt% SiC; then, the wear rate gradually increased. The wear rate of the counter-bodies had an equivalent behavior. It is also noticeable that despite the higher hardness, the counter bodies had a much higher wear rate than the specimens (one order of magnitude), Fig. 3.21b.

There is a complex competition among different phenomena:

(i) During the silicon carbide dissociation, the matrix hardened because of the Si diffusion, which increased the strength of the composite. However, the mechanical strength decreased because graphite nodules and pores (4–12% [59])
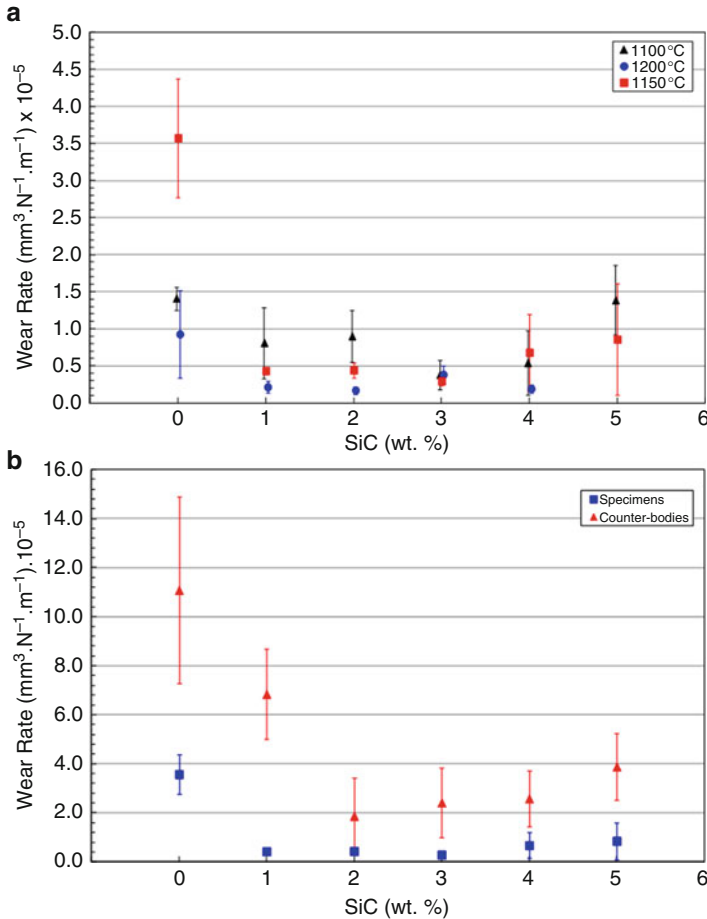
Fig. 3.21 Wear rate. (**a**) Effect of the SiC content and sintering temperature on the wear rate of the specimens. *The x values were slightly shifted* (± 0.02) *to the left and to the right in order to separate overlapping symbols*). (**b**) Evolution of the wear rate of the specimens (sintering temperature = 1150 °C) and counter-bodies as a function of the SiC content

formed during the sintering process, which decreased the degree of continuity of the metallic matrix [69].

(ii) The graphite nodules formed a protective tribolayer at the interface, which led to the better tribological behavior of the composites.

Composites with SiC amounts exceeding 4 wt% featured an increased wear rate, which may be associated with a decreased mechanical strength due to the large amount of pores/graphite nodules (large discontinuity of the matrix) [59], as illustrated in Fig. 3.11b, c. In this case, the graphite nodules decreased the hardness and increased wear despite the presence of a rich carbon-based protective layer in the contact interface, which is responsible for the low friction coefficient (Fig. 3.20).
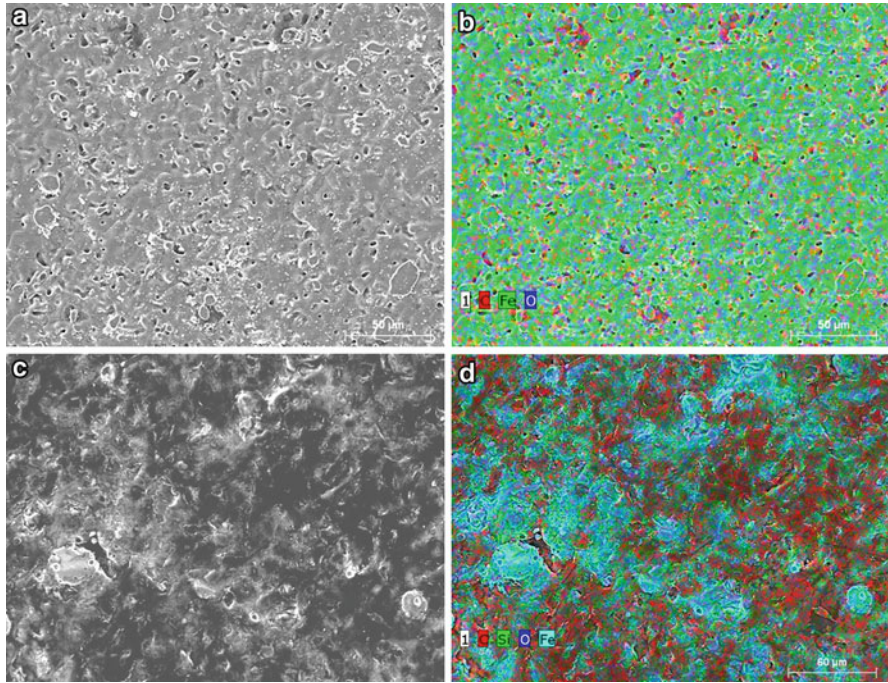
Fig. 3.22 Typical SEM images and elemental mapping of specimen surfaces before the tests. (**a**, **b**) Matrix alloy (Fe-0.6 wt% C); (**c**, **d**) composite Fe-0.6 wt% C + 3 wt% SiC

Figure 3.22 shows the typical SEM and elemental mapping images of the specimen surfaces before the tests. It is noticeable that the matrix alloy exhibited a slightly higher porosity. Moreover, the use of SiC as a precursor for the graphite nodules was notably efficient. In fact, the elemental mapping images clearly show large amounts of carbon (red regions) well distributed on the composites surfaces.

Figure 3.23 shows typical aspects of the surfaces after the tests and illustrates the wear mechanisms that acted on the specimens and counter-bodies. For the matrix alloy (Fig. 3.23a), the wear marks have smoother surfaces where third-body "islands" (arrow) are observed. Moreover, third-body islands are also visible in notably smooth and even counter-body worn surface, which are indicated with an arrow in Fig. 3.23b. The EDX analysis of these regions [76] shows that they are rich in oxygen.

Surprisingly, unlike the observation in the reference sample, composites with graphite nodules in the microstructure (3 and 5 wt% SiC) show strong evidence of plastic deformation, Fig. 3.23c, which is characterized by the presence of grooves parallel to the sliding direction, which indicates abrasive wear as the dominant wear mechanism. This aspect is even more evident in the wear marks of the counter-bodies, Fig. 3.23d.

A great quantity of wear debris was observed on the wear marks. Figure 3.24 shows the general aspect, morphology, and dimensions of the produced particles.
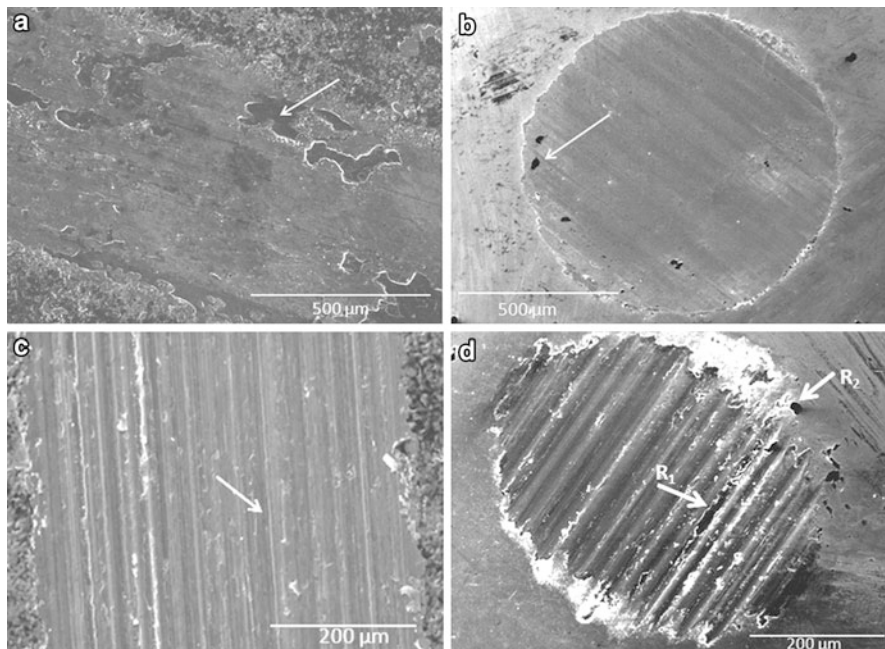
Fig. 3.23 Typical wear mechanisms. (**a**) Matrix alloy, specimen; (**b**) matrix alloy, counter-body; (**c**) 3 wt% SiC composite, specimen; (**d**) 3 wt% SiC composite, counter-body
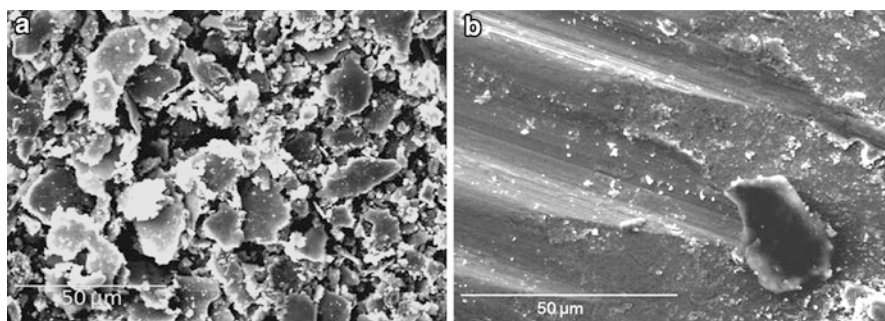

Fig. 3.24 Wear debris. (**a**) General aspect; (**b**) producing abrasion on the counter-body. Composite Fe-C- 3 wt% SiC

They consist primarily of carbon and oxygen, as evidenced by EDX. It is reasonable to assume that these particles actively operate in the abrasion process, as clearly shown in Fig. 3.24b.

The chemical composition analysis using EDX [76] in the regions indicated with arrows in Fig. 3.23 shows the presence of oxygen and an important carbon content in the wear mark of the samples. Even if the strong abrasion apparently does not allow for tribolayer formation, a significant amount of carbon (approximately 20 wt%) was
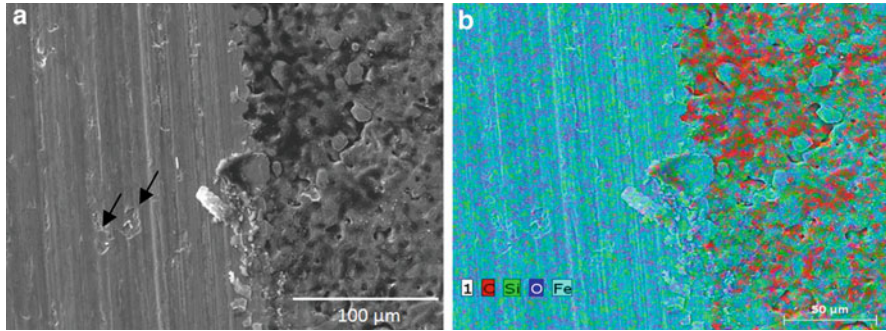
Fig. 3.25 Wear scar. (**a**) Typical aspect at the boundary; (**b**) X-ray map obtained using EDS. Composite Fe-C- 3 wt% SiC
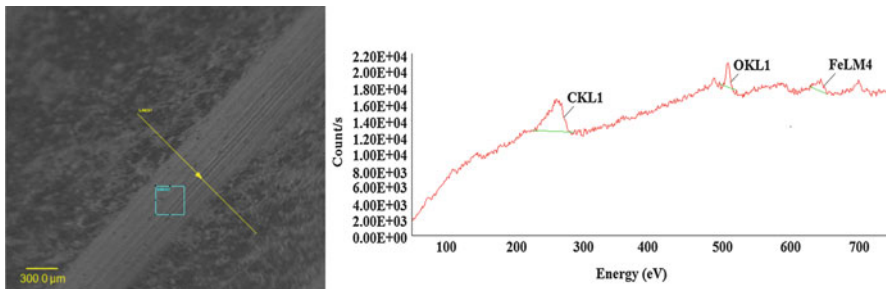

Fig. 3.26 Typical AES analysis. Fe-C- 3 wt% SiC composite

found in the wear mark of the counter-body (regions R_1 and R_2, Fig. 3.23d), which proves the existence of a carbon-rich material.

A high magnification analysis (Fig. 3.25a) shows a tenuous tribolayer that is fractured at various points.

By associating this image with the map of elements obtained using EDX (Fig. 3.25b), it is possible to verify that the contact is fuelled by carbon from the graphite nodules. Furthermore, oxygen is observed (dark blue region), which was expected because the tribological tests were performed in air.

To further understand this point, the wear scar of the 3 wt% SiC composite was analyzed using Auger electron spectroscopy (AES), Fig. 3.26.

Analyses in the wear scar confirmed that the tribolayer, which was formed during sliding, was composed of oxygen and predominantly carbon. In contrast, a similar analysis performed on the wear marks of the reference sample (matrix alloy) [76] showed the predominance of oxygen in the worn surface, which indicates the presence of oxides in the tribolayer.

To further understand the formation and degradation of the tribolayer, using the 3 wt% SiC composite as specimens, sliding tests were conducted and interrupted at predefined moments, corresponding to 100, 1000, and 2000 cycles.
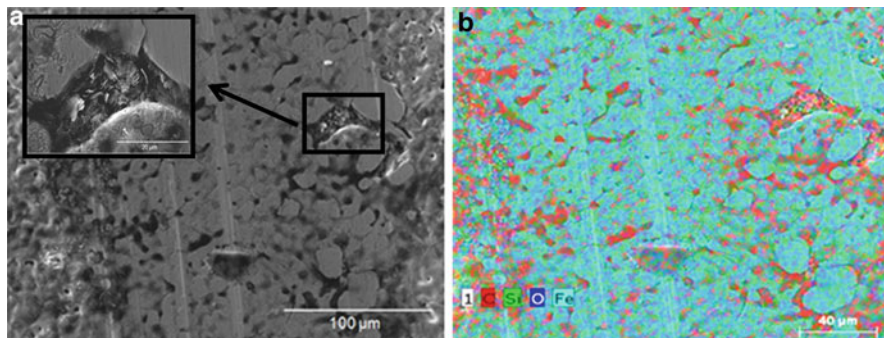
Fig. 3.27 Wear scar after 100 cycles: (**a**) SEM images and (**b**) elemental analyses

Figure 3.27 shows the typical aspects of the wear scar after 100 cycles.

The pores in the samples were filled with lamellar structures, as shown in the high-magnification inset in Fig. 3.27a. The elemental map shows that this material is rich in carbon, which was confirmed using the EDX analysis (~31 wt% C). It is reasonable to suppose that the graphite foils are removed from the in situ-generated graphite nodules and remain at the interface, which contributes to the formation of the protective tribolayer interface.

However, despite the presence of a few scratches, the surface of the counter-body had a large amount of carbon (~30 wt%), which indicates material transfer during the test and the early formation of a graphite-rich tribolayer at the contact interface, which maintained the region lubricated and reduced the coefficient of friction at the end of 100 sliding cycles.

The main features associated with longer test times (1000 and 2000 cycles) were pore closure and tribolayer degradation. Figure 3.28 illustrates the typical aspects of the wear scars after 1000 cycles.

The strong plastic deformation that led to the pore closure at the center of the wear scar was evidently associated with the tribolayer spalling. Additionally, EDS chemical analyses showed the presence of carbon and oxygen. Furthermore, the oxidation processes associated with tribochemical reactions contributed to the formation of oxide regions on the counter-body surface.

Effect of Surface Finishing

In this section, the influence of surface finishing (as sintered and polished) on the tribological behavior of MIM self-lubricating composites sintered at 1150 °C with (3 and 5% wt%) and without SiC additions is presented. The tribological behavior was analyzed using linear reciprocating sliding tests (constant load of 7 N, 60 min duration). Polishing of the specimens was performed manually with sand paper #1200, #2400, and #4000 in a polishing machine with automatic controls of time and rotation, for 10 min and 150 rpm. After polishing, the surface topography was characterized.
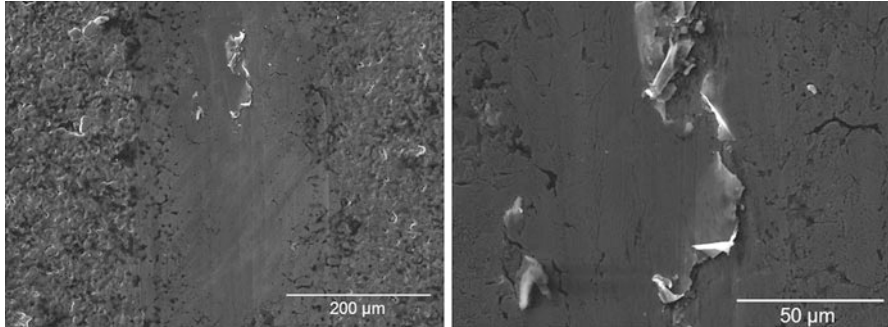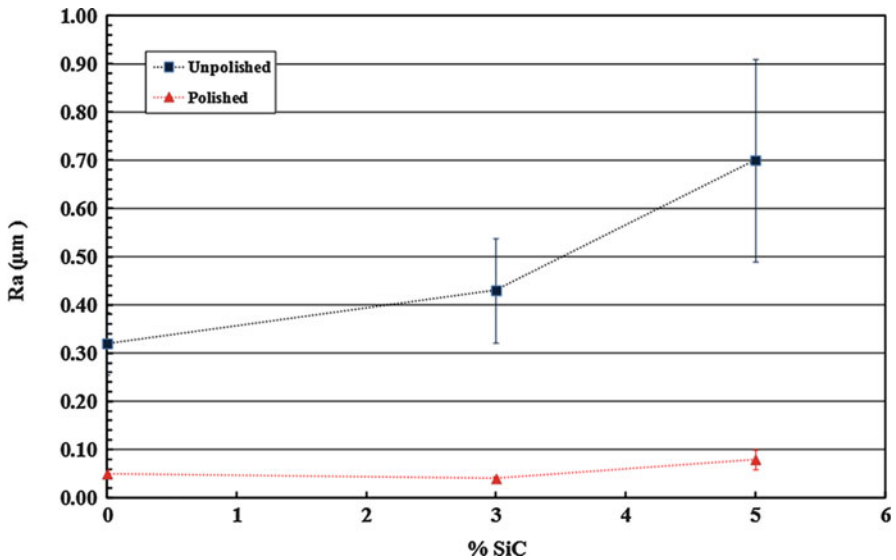
Fig. 3.28 Wear scar after 1000 cycles

Fig. 3.29 Average surface roughness according to SiC content before and after polishing

The effect of SiC content on surface topography before and after polishing is illustrated in Fig. 3.29.

The mean surface roughness of unpolished samples increases significantly when the SiC content increases. Such behavior can be observed also for polished samples, but in a more subtle way. As already mentioned, the reference alloy presented a microstructure constituted of perlite + ferrite whereas the addition of SiC induces the formation of 2D turbostratic graphite nodules which in turn induced increased surface roughness. Thus, higher SiC contents increase the quantity of graphite nodules and, therefore, increase surface roughness. After polishing, a significant reduction of the average values of Ra is observed when compared with the values obtained for the unpolished samples.

Typical aspects of the surfaces before and after polishing are presented in Fig. 3.30.
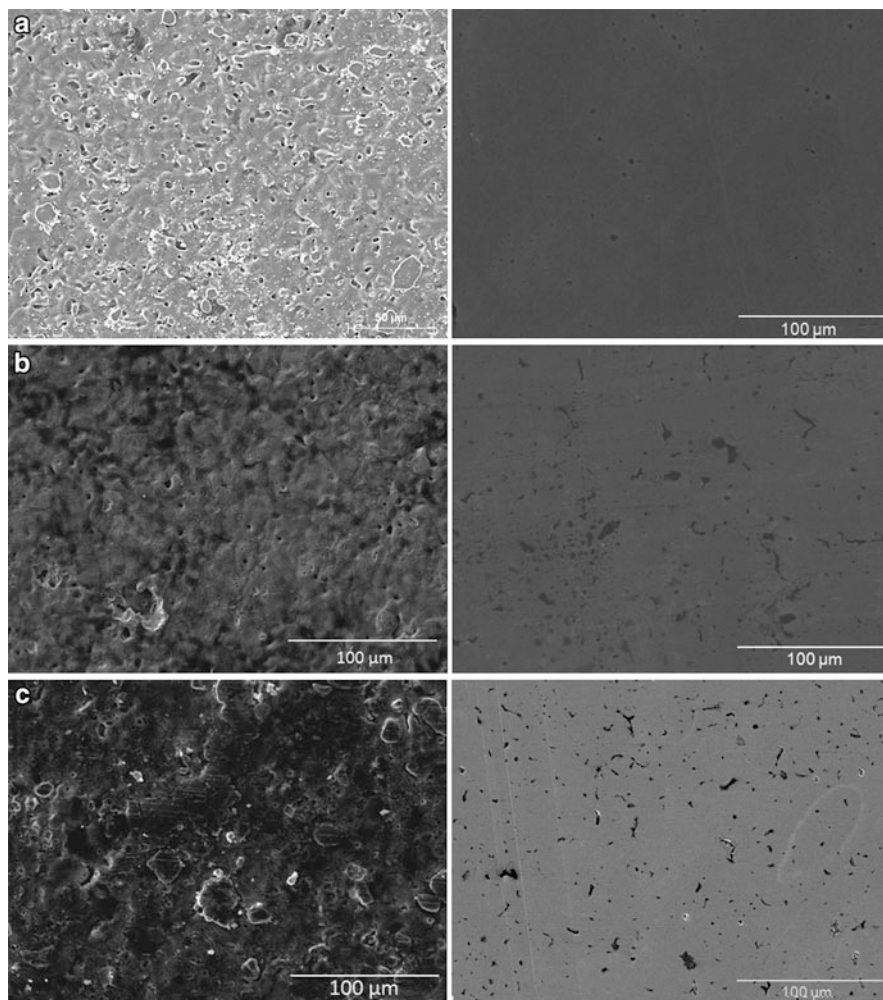
Fig. 3.30 Typical surfaces of unpolished surfaces (left) and polished (right) specimens. (**a**) 0 wt% SiC; (**b**) 3 wt% SiC and (**d**) 5 wt% SiC

It is clearly observed that after polishing the surfaces are smoother and feature dark regions constituted of graphite nodules and pores. From now on, these dark regions will be called lubricant reservoirs. Due to limitations of the technique used for image analysis already reported in the literature [59, 61], it was not possible to distinguish between pores and graphite nodules. The dark regions were previously identified as turbostratic 2D graphite. Compared with the polished surface of the reference sample (0 wt% SiC), the polished surfaces of specimens containing 3 and 5 wt% SiC presented increasing amounts of dark regions (pores + graphite nodules) evenly distributed on the surface.
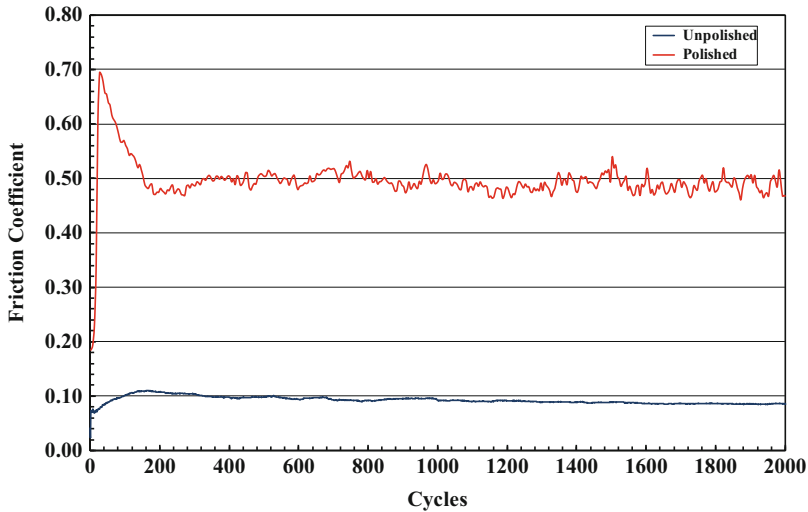
Fig. 3.31 Typical evolution of friction coefficient with number of cycles. 3 wt% SiC

Figure 3.31 shows how the evolution of the friction coefficient during the test duration is influenced by surface finishing.

All results present similar behavior. There is a transient associated with the onset of contact between specimen and counter-body at the beginning of tests before a steady state is reached. For the unpolished specimens, friction coefficient showed a rapid increase and stayed nearly constant during the rest of the test, i.e., a steady state was reached. For the polished specimens, after a rapid initial increase, friction coefficient starts to gradually decrease to a lower steady-state value.

As already discussed the reasons for the difference in the evolution of the friction coefficient within the transient period will not be treated in the present chapter. However, it is reasonable to suppose that the stabilization of the friction coefficient is related to the generation of a protective tribolayer, where the transient corresponds to the kinetics of formation of the layer. The values of the friction coefficient for each test were computed by averaging the steady-state values. The results are summarized in Fig. 3.32.

Increasing the precursor content and, as a consequence, the number of turbostratic 2D graphite nodules produced a reduction of the average friction coefficient. In general, the reduction was substantial, up to 3% SiC. For higher values of SiC content, the friction coefficient was almost constant. As already stated, the graphite foils are removed from the in situ-generated graphite nodules and remain at the interface thus contributing to the formation of the protective tribolayer.

Additionally, it is observed that the friction coefficient is strongly influenced by surface finish. Polished specimens exhibit significantly higher friction coefficients ($\mu > 0.4$) suggesting that the 2D turbostratic graphite nodules do not actively participate in the tribolayer formation. In fact, multielemental X-ray maps obtained
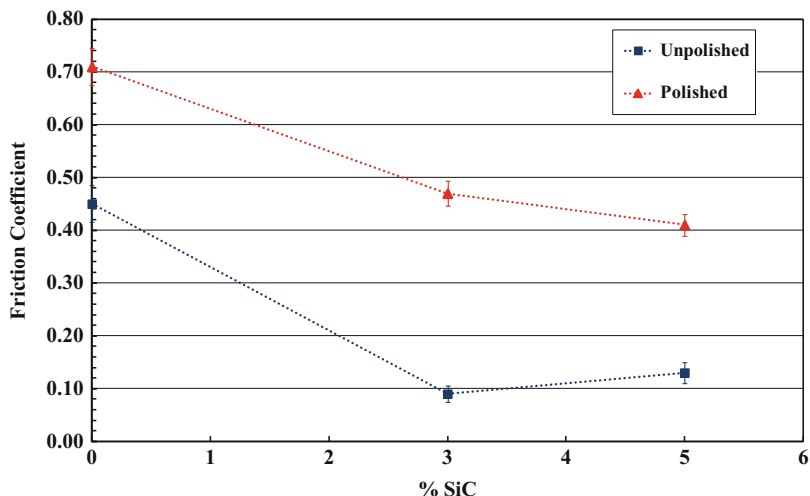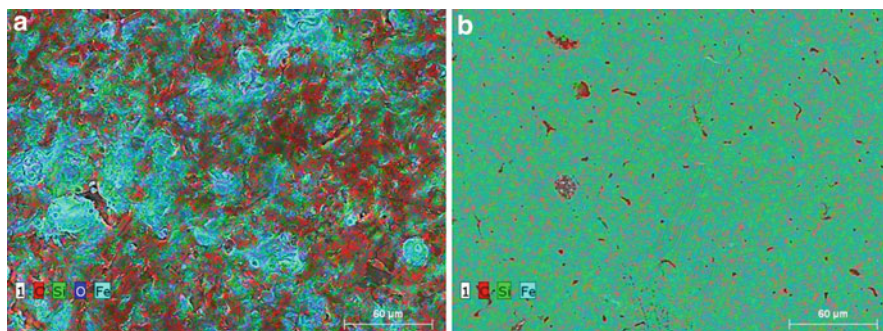
Fig. 3.32 Steady-state friction coefficient

Fig. 3.33 Multielemental X-ray map obtained by EDS. Composite Fe-0.6% C-3% SiC. (**a**) Unpolished. (**b**) Polished

by EDS (Fig. 3.33), in which the red color is associated with carbon, clearly show a large decrease in the amount of graphite nodules for the polished surface.

Besides significantly reducing the surface roughness, as illustrated in Figs. 3.29 and 3.30, polishing also affected the availability of solid lubricant reservoirs in the active sliding interface. It is well known the paramount role played by pores (in our case pores + solid lubricant reservoirs) in the tribological behavior of sintered materials [39, 78].

In addition to a reduction in strength and, as a consequence, in load bearing capacity, the presence of porosity alone might influence the wear mechanisms acting on the surfaces of powder metallurgy parts in a number of ways. In particular, open pores in the active interface are reported to act as foci for the generation and trapping
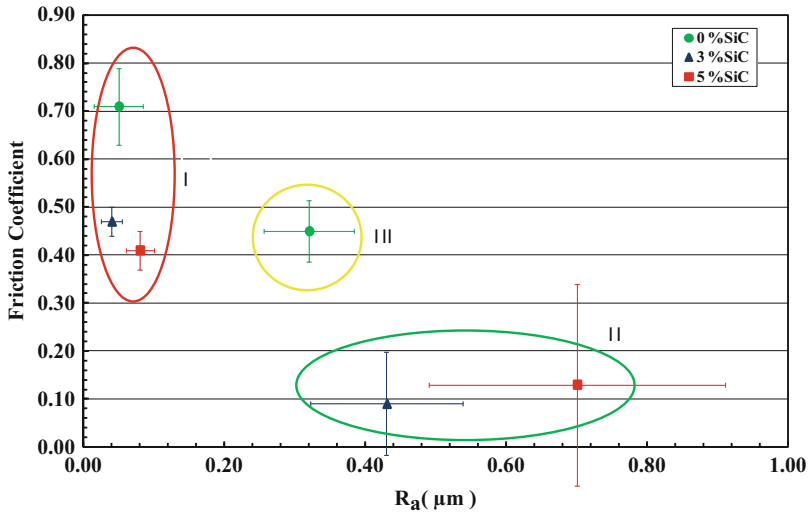
Fig. 3.34 Friction coefficient in function of surface roughness and SiC content

of wear debris during sliding wear [77]. If the reservoirs remain active (open), there will be a continuous self-replenishment of solid lubricants to the contact area and, as a consequence, the maintenance of a protective tribolayer [45]. The plastic deformation imposed by polishing induces the closure of pore + solid lubricants reservoirs, which significantly reduces the lubricant supply into the active interface. This justifies the high friction coefficient presented by the polished composites. Without a doubt, the closure of the reservoirs is an important factor in increasing friction coefficient of the composites containing SiC. On the other hand, it would not justify the increased friction coefficient also observed for the reference composites alloys (without SiC) since they do not contain graphite nodules. In this case, it is reasonable to suppose that the variation in friction coefficient is mainly due to changes in surface topography during polishing.

In addition, friction coefficient decreased when the amount of precursor (SiC) increased for both surface finishing routes. The reference specimen (0% SiC) presented a mean friction coefficient significantly higher than those of the samples containing 3% and 5% SiC. It is remarkable the positive influence of turbostratic 2D graphite nodules on the tribological behavior of these composites. For the case of the unpolished specimens, the addition of 3% SiC induced a remarkable 80% reduction in friction coefficient.

There is a compromise between surface topography and solid lubricant availability in the active interface. Figure 3.34 shows the average friction coefficient as a function of roughness. Three regions are highlighted in Fig. 3.34: The first region (I) consists of the polished samples (0%, 3%, and 5% SiC); the second region (II) is associated with unpolished samples containing 2D turbostratic graphite nodules (3% and 5% SiC), and finally, the third region (III) concerns the unpolished reference alloy (0% SiC).

The polished samples, regardless of the chemical composition, showed higher friction coefficients and obviously low roughness when compared with the unpolished ones. On the other hand, the unpolished composites (region II) presented higher roughness associated with lower friction coefficient. Also noteworthy is the unpolished reference alloy behavior (region III): It presents intermediate values for both roughness and friction coefficient, suggesting the already mentioned compromise between surface topography and solid lubricant availability in the active interface suggesting that the presence of 2D turbostratic graphite nodules affects the surface topography of the samples and has a great influence on the dynamics of the formation of protective tribolayers, and consequently on wear mechanisms [69, 78]. In fact, the polished samples, regardless of the chemical composition, presented very low values of reduced valley height (Rv) (0.1–0.18 μm) when compared with the unpolished ones (0.67–1.51 μm). Since Rv is related to the distribution of valleys or pores in a surface [79], this evidences the closure of pores + solid lubricant reservoirs during polishing.

According to Keller et al. the difference in surface topography has an important impact on wear mechanisms and building up of tribolayers [79]. A rough surface, i.e., small real contact area or high real contact pressure, leads to higher friction coefficients and wear [79]. However, despite being considerably rougher than the polished specimens, the unpolished specimens presented significantly lower friction coefficients, pointing to an important participation of the turbostratic graphite nodules in the lubrication process. It appears that during sliding, due to the high contact pressure, the formation of the protective tribolayer occurs rapidly in the initial cycles, preventing direct metal-metal contact, and thus maintaining low friction coefficients. If the reservoirs remain active (open), there will be a continuous self-replenishment of solid lubricants to the contact area and, as a consequence, the maintenance of a protective tribolayer as illustrated in Fig. 3.35 which shows a kind of self-healing feature of the tribolayer. Whenever the normal force is increased (black curve) there is a partial destruction of the tribolayer as indicated by the sharp decrease in electrical potential of the contact. Immediately, the tribolayer is reestablished as clearly indicated by the rapid increase in electrical potential of the contact.

Figure 3.36 presents the influence of the precursor content and of the specimen surface finish on the wear rates of the specimens and their respective counter-bodies.

The influence of surface finish was marginal for the reference alloys (0% SiC). However, for the composites (3% and 5% SiC), the unpolished specimens exhibited significantly lower wear rates compared to the polished samples, Fig. 3.36a.

The counter-bodies (Fig. 3.36b) presented much higher wear rates when siding against the polished surfaces, being this even more significant for the reference alloy (0% SiC). The absence of graphite nodules associated with the smooth surface topography of the reference samples promoted an increased wear of the specimen and respective counter-bodies. Polishing, besides modifying the surface topography of the sample, promoted the closure of the pores and of the graphite reservoirs as already described. This resulted in increased friction coefficient and wear rates for both sides of the tribo pair.
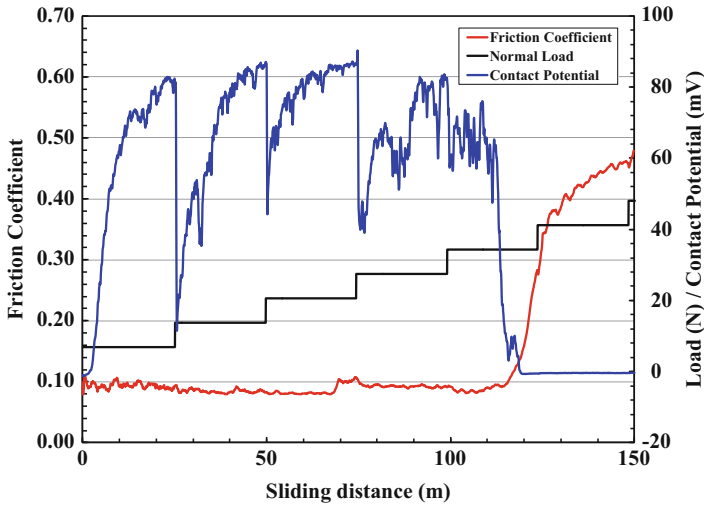
Fig. 3.35 Self-healing of the tribolayer

Typical aspects of the wear scars of specimens and counter-bodies associated with polished specimens are shown in Fig. 3.37. In both cases, there are clear indications of abrasive wear. For the reference alloy, analysis by EDX in selected areas indicated a strong presence of oxygen in the active interface of both specimens (30%) and counter-bodies (14%), a clear evidence of oxidative wear [76].

Abrasive wear evidence is even more visible in wear scars associated with specimens rich in 2D turbostratic graphite, Fig. 3.38.

Moreover, EDX analysis indicated the presence of a protective tribolayer in the wear scars of both specimen and counter-body, as indicated by the higher amounts of carbon (specimen: 9%; counter-body: 14%) in relation to the reference alloy.

Again, a great quantity of wear debris was observed on the wear marks. Elemental analysis by EDX of the wear debris [76] showed that the debris generated for the reference alloy have higher oxygen content than the debris produced by the composites containing 2D turbostratic graphite nodules which, in turn, are richer in carbon. During sliding in air, oxygen reacts at the contact interface giving rise to a tribolayer that forms and breaks down cyclically. For the reference alloys, the rupture of this tribolayer gives rise to wear debris consisting mainly of iron and oxygen. The debris originated from the composites, in addition to iron and oxygen, also present, as expected, a significant amount of carbon, since the graphite nodules actively participate in lubrication of the contact interface, thereby justifying the low friction coefficients and wear rates measured for the unpolished samples.

Effect of the Metallic Matrix
Apart from contributing to the formation and degradation of the tribolayer, the microstructure of the metallic matrix always has large influence on the tribological
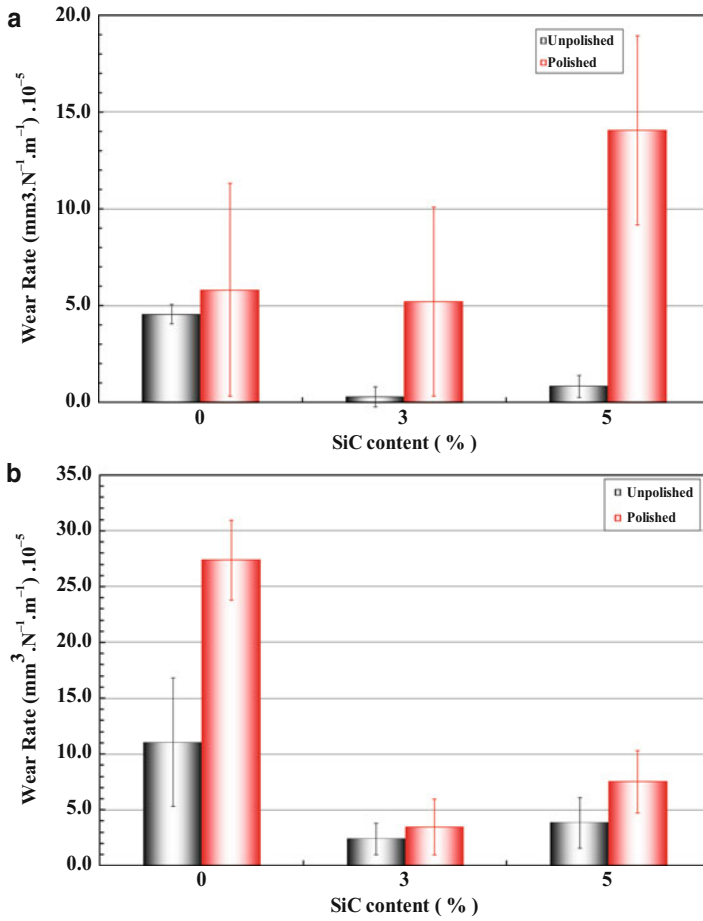
Fig. 3.36 Wear rate. (**a**) Specimens. (**b**) Counter-bodies
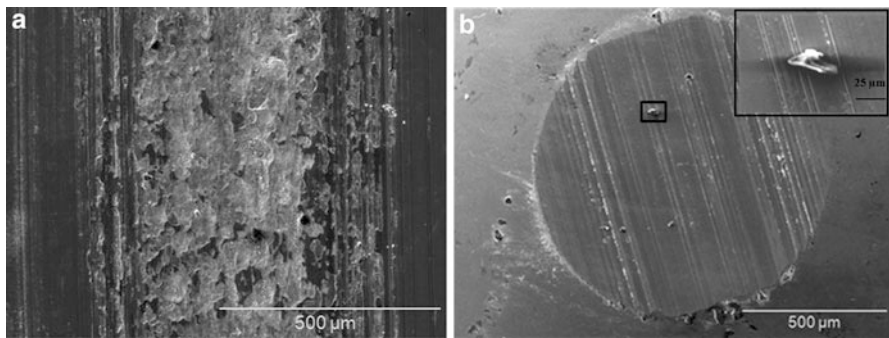

Fig. 3.37 Typical aspects of the wear scars. Reference alloy (0% SiC) (**a**) polished specimen. (**b**) Counter-body
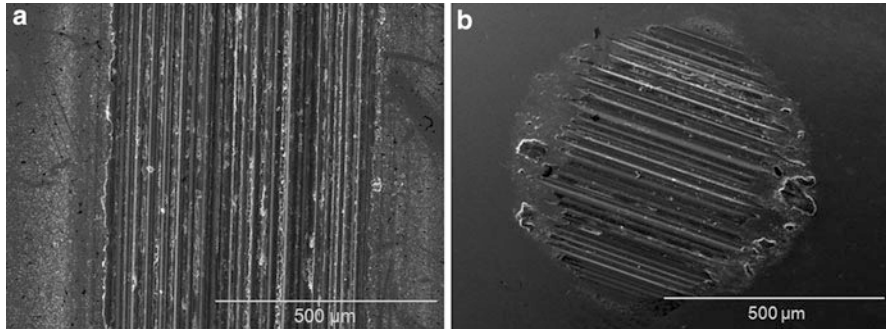
Fig. 3.38 Typical aspects of the wear scars. 3% SiC composite (**a**) polished specimen. (**b**) Counterbody

behavior of any material. According to Zum Gahr [80], when considering wear, the best tribological behavior of a metallic material is reached by combining the most appropriate combination of strength, ductility, and fracture toughness.

In this section, the effect of the metallic matrix composition on the formed microstructural constituents, as well as their effect on the tribomechanical behavior of plasma-assisted debinded and sintered MIM self-lubricating composites is presented and discussed. Three different metal matrices containing embedded 2D turbostratic graphite nodules were obtained by adding alloying elements (Ni and Ni + Mo) to the initial composition of the Fe-C-SiC composite.

Figure 3.39 illustrates the typical microstructures of the studied composites.

All composites were prepared by mixing 3% SiC to the feedstock and were sintered at 1150 °C for 1 h. All three microstructures have in common the presence of graphite nodules (arrows), induced by the addition of SiC to the feedstock powder, whereas for the present imposed conditions, the metallic matrix varies from ferrite to martensite. Addition of Nickel did not substantially change the microstructural constituents (ferrite + small fractions of perlite), Fig. 3.39b, but it seems that the graphite nodules are a little larger and in greater quantities than in the standard Fe-C-composites. For the Ni + Mo containing composite, the metallurgical constituents changed from ferrite/perlite to martensite even under the low cooling rates imposed by the PADS reactor (7 °C/min). The addition of these elements probably dislocated the TTT curve of this steel, favoring the formation of martensite [81].

Figure 3.40 summarizes the mechanical properties of the composites.

They were evaluated by measuring the micro-hardness of the metallic matrix and the tensile resistance of the composite (elongation, yield strength, and ultimate strength). It is possible to observe that even with the presence of solid lubricant nodules in the metallic matrices, the level of resistance for the composites is very high. This occurs because the nodules of graphite are very small (less than 20 μm) and they are homogeneously dispersed throughout the ferrous matrix thus preserving the matrix continuity.

As expected, the addition of alloying elements produced a strong effect on the hardness and mechanical strength of the matrices. Nickel increases the resistance of
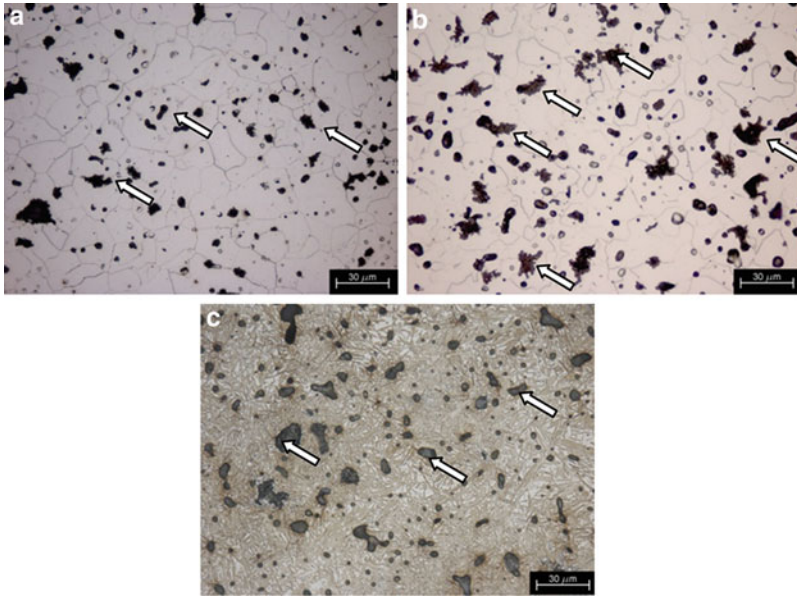
Fig. 3.39 Typical microstructure of self-lubricating composites produced by adding 3% SiC. (**a**) Fe + 0.6%C. (**b**) Fe + 0.6%C + 4.0%Ni. (**c**) Fe + 0.6%C + 4.0%Ni + 1.0%Mo

Fig. 3.40 Mechanical properties

the composites by solid solution and partially reduces its ductility in relation to the standard Fe-C composite. The combination of Ni + Mo induces a large increase in mechanical resistance because it changes the metallurgical microstructure from ferrite/perlite to martensite. As explained earlier, the martensite transformation

occurs for the Fe-C-Ni-Mo even under low cooling rates. As expected, the elongation behaved in a contrary manner.

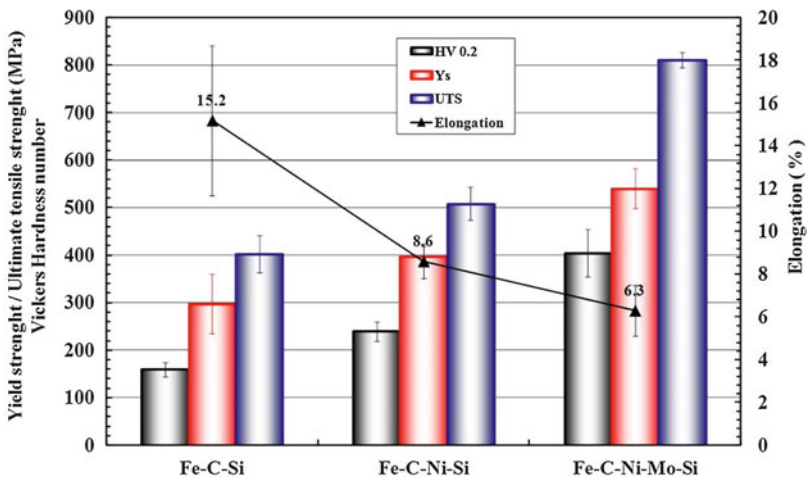It is worth noting that UTS values as high as 1000 MPa were reported for the Ni + Mo containing composite when sintered at 1200 °C [61]. A possible factor for such an increase in mechanical properties was the higher homogenization obtained at higher temperatures. It is very well known that the diffusion rates are enhanced with temperature. Furthermore, at 1200 °C, liquid phase sintering may occur, thus producing a better chemical homogenization and densification.

It might also be interesting to point out that the UTS of self-lubricating composites available on the market do not normally exceed 300 MPa. This is a result of the large discontinuity of the metallic matrix produced by the addition of up to 40% of large solid lubricant particles which are necessary to keep friction at low levels.

The friction coefficient of the reference composite (Fe-C) gradually increases with the sliding distance until, at about 100 m, it evolves in a more uniform and constant way. For the composites containing nickel and molybdenum, the friction coefficient evolves in a more stable way from the beginning of the test. Although presenting a significantly lower average value, the evolution alternates low and high intensities periods. Furthermore, a higher oscillation of the contact potential was verified, indicating instability of the insulating tribolayer. The Ni-containing composites presented a similar evolution at values in between those of the reference composite and that of the Ni-Mo composites [82].

The effect of metallic matrix composition on the steady-state friction coefficient is presented in Fig. 3.41.

The reference composite, Fe-C, presented the highest friction coefficient (0.11). The addition of alloying elements considerably reduced the friction coefficient (45% reduction for the Ni composites) and values as low as 0.04 (65% reduction) for the Fe-C-Ni-Mo composites. This remarkably low value may be considered superlubricity in the real world.

Figure 3.42 illustrates the general appearance of the wear scars produced in both specimens and counter-bodies.

Wear scars associated with the specimens presented different widths and the general appearance of the wear marks also varied. The wear volume was reduced by the introduction of the alloying elements. Inside the wear scar there is a clear evidence of abrasive wear, as evidenced by the presence of multiple parallel scratches. The intensity and number of scratches varied according to the material. The wear loss of the counter-bodies (AISI 52100 steel ball) presented the same behavior as the specimens. The wear rate of specimens and counter-bodies is summarized in Fig. 3.43.

The lowest wear rate value determined was 8.29×10^{-6} mm^3 N^{-1} m^{-1} for the Fe-C-Ni-Mo composites whereas the highest wear rate was measured for the reference composite (Fe-C), 34.5×10^{-6} mm^3 N^{-1} m^{-1}. This corresponded to a 420% reduction. For the nickel composites (14.5×10^{-6} mm^3 N^{-1} m^{-1}), the reduction was 240% in relation to the reference composite. In all cases, the wear rate of the ball was almost identical [(9.47; 19.31 and 37.22) $\times 10^{-6}$ mm^3 N^{-1} m^{-1}, respectively] which induced the same order of magnitude in wear reduction.
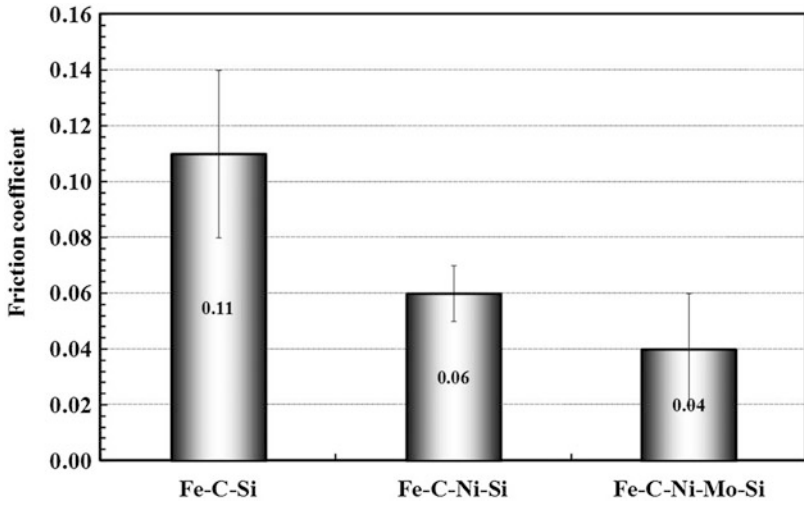
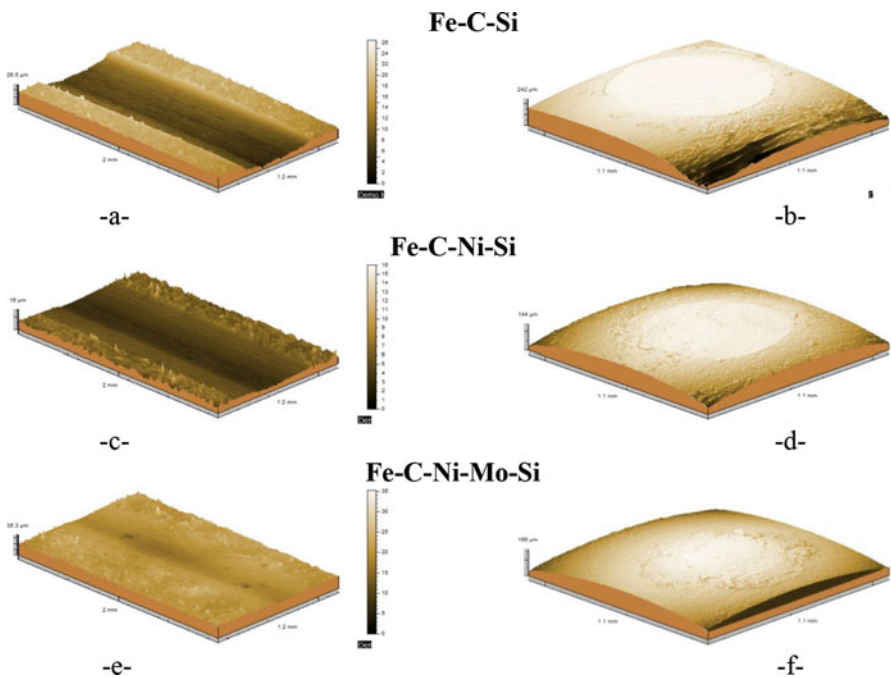**Fig. 3.41** Steady-state friction coefficient

Fig. 3.42 Typical aspects of the wear scars obtained by laser interferometry. Composite Fe-C-Si, (**a**) specimen, (**b**) counter-body. Composite Fe-C-Ni-Si, (**c**) specimen, (**d**) counter-body. Composite Fe-C-Ni-Mo-Si, (**e**) specimen, (**f**) counter-body
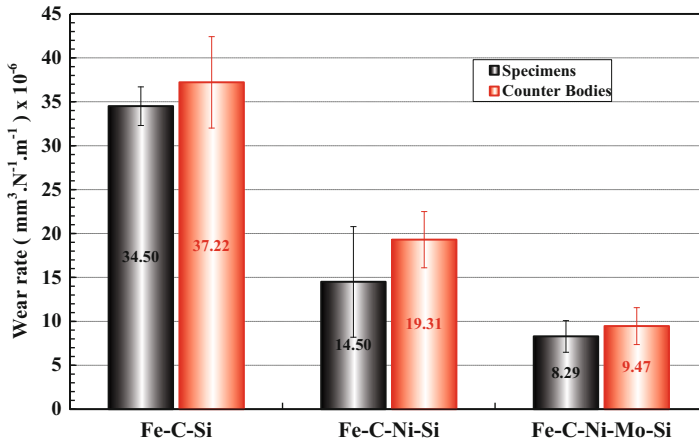
Fig. 3.43 Wear rate of the self-lubricating composite and AISI 52100 steel ball
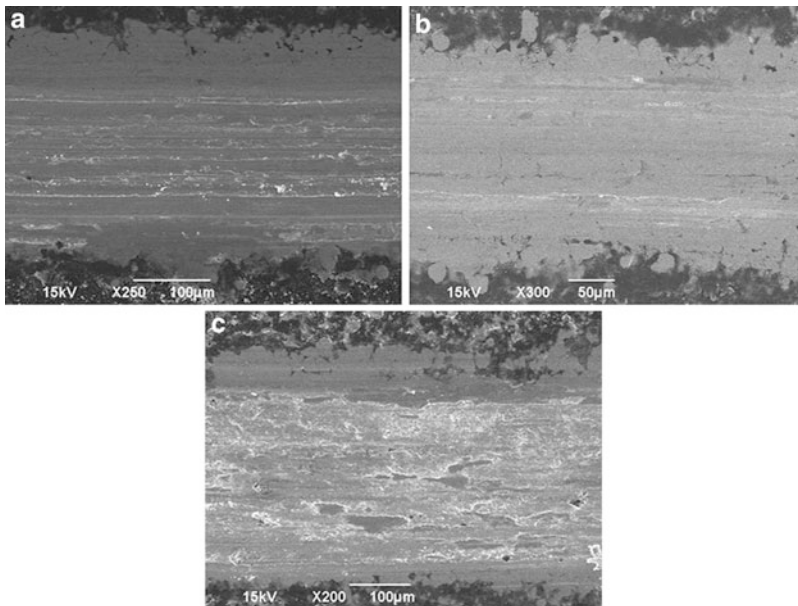
Fig. 3.44 General appearance of the wear scars. (**a**) Fe-C. (**b**) Fe-C-Ni. (**c**) Fe-C-Ni-Mo

Figure 3.44 illustrates the general appearance of the wear scars produced.

Wear mechanisms acting on the reference composite and on the nickel-containing composite are quite similar: Abrasive wear is present as indicated by the fine scratches in the sliding direction. The intensity and number of scratches varies according to the material. The shallow, thinner, and less numerous scratches are present in Fe-C-Ni specimens. They are probably caused by the abundant hard,

Fig. 3.45 Selected appearance of the wear scars. (**a**, **b**) Fe-C-Si composite. (**c**, **d**) Fe-C-Ni-Mo-Si composite

oxidized wear debris generated at the interface. On the other hand, for the nickel-molybdenum composite the tribological conditions produced smoother surfaces where third-body "islands" were observed.

This behavior might be linked to the resistance of the metallic matrix to plastic deformation and consequently, to the sealing of lubricant reservoirs, Fig. 3.45.

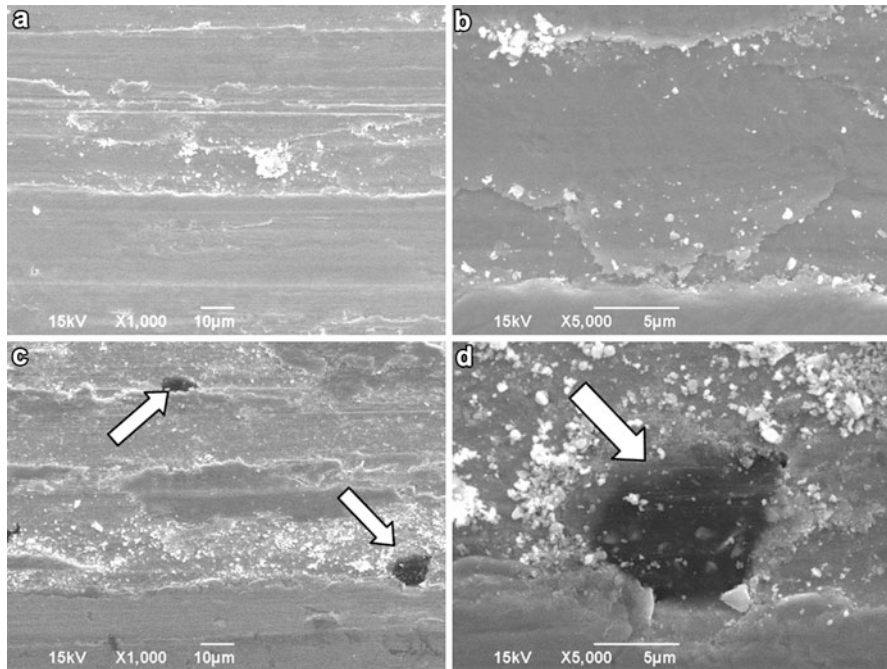For the higher friction coefficient and wear rate specimens (Fe-C composites, Fig. 3.45a, b), the intense plastic deformation produces the complete closure of the solid lubricant reservoirs, whereas for the lower friction coefficient and wear rates (Fe-C-Ni-Mo composites, Fig. 3.45c, d), the solid lubricant reservoirs remains open and active (white arrow).

If the solid lubricant particles do not reach the surface, the self-replenishment mechanism of the tribofilm is partially restrained and the friction coefficient remains relatively high.

In order to further understand the effect of the metallic matrix on the tribolayer (and, as a consequence, on the tribological behavior), the wear scars present on the specimens and counter-bodies were analyzed by micro-Raman spectroscopy. Figure 3.46 synthesizes these results.

Again, only the borderline results are presented: Fe-C samples (higher friction coefficient and wear rates) and Fe-C-Ni-Mo composites (lower friction coefficient and wear rates).
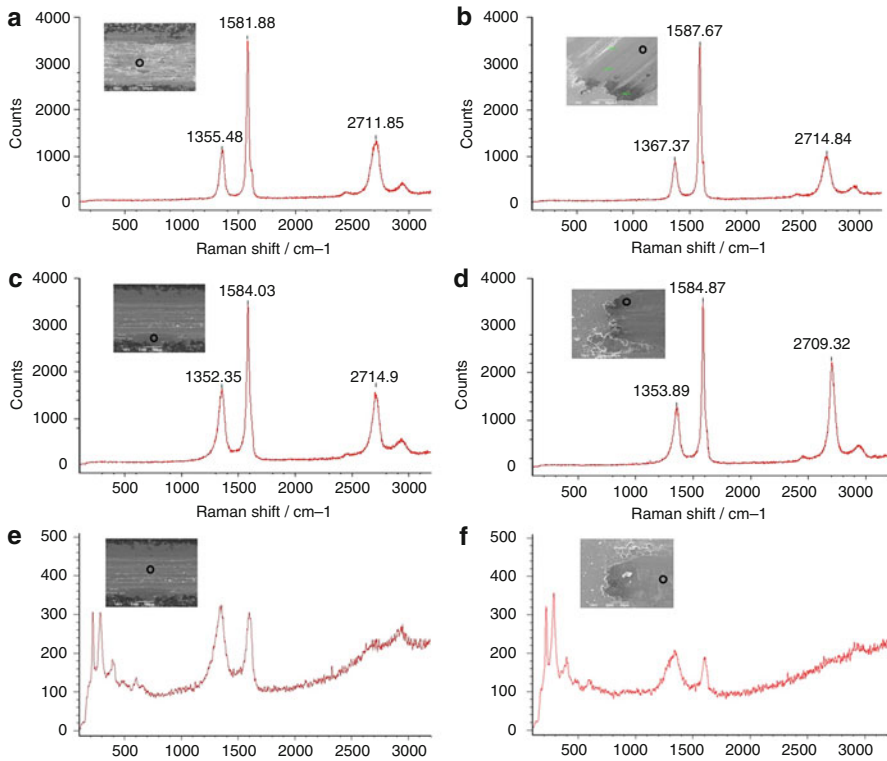
Fig. 3.46 Typical Raman spectra. (**a**) Fe-C-Ni-Mo specimen. (**b**) Fe-C-Ni-Mo counter-body. (**c**) Fe-C specimen, border of the scar. (**d**) Fe-C counter-body, border of the scar. (**e**) Fe-C specimen, center of the scar. (**f**) Fe-C counter-body, center of the scar

Figure 3.46a, b present the dominant spectra found in the wear scar of the Fe-C-Ni-Mo composite. All spectra clearly show the presence of the so-called turbostatic 2D graphite as evidenced by the typically widened G band and the presence of a D band which is associated with crystallinity disorder. The measured widening of the bands, the ID/IG ratio, the size of the graphite crystallites, and the analysis of the second-order band G′ also confirm the disorder in the material. It is also noticeable that the spectra of tribolayers presented in the wear scars of the specimens or in the counter-bodies are almost identical and indicate the beneficial presence of the turbostatic 2D graphite on both sides of the tribo pair.

On the contrary, the spectra found in the wear track of the reference composite changed according to their position in the wear scar. Spectra similar to those found in the previous case were measured near the border of the wear scars, Fig. 3.46c, d whereas those found in the center of the scar were a little different, Fig. 3.46e, f. Despite presenting lower intensities of the 2D graphite characteristic bands and a certain amount of fluorescence, the spectra also presented other smaller bands at lower frequencies. The origin of these bands was attributed [13] to the formation of

Table 3.1 Relevant properties

Property		MIM + PADS + In situ
Scuffing resistance [N m]		8000
Friction coefficient		0.04
Wear rate [mm^3 N^{-1} m^{-1}] · 10^{-6}	Specimen	8.28
	Counter-body	9.47
Ultimate tensile strength [Mpa]		500
Elongation [%]		6.3

iron oxide by tribochemical reaction caused by the surrounding atmosphere and is, probably, a consequence of the high energy availability associated with high friction coefficients. The positions of the bands in the range of 225–650 cm^{-1} match fairly well those observed for iron oxide phases [83].

The bands at 290, 408, 497, and 607 cm^{-1} indicated the presence of hematite Fe$_2$O$_3$ whereas the band at 667 cm^{-1} was assigned to magnetite Fe$_3$O$_4$ [84–86]. It is reasonable to suppose that the presence of iron oxides associated with the smaller intensities of the graphitic phase is likely to induce inferior tribological performance.

3.8   Concluding Remarks

We introduced a new microstructural model/processing route (metal injection molding followed by a single thermal cycle using a plasma-assisted debinding and sintering process and in situ formation of graphite nodules due to the dissociation of a precursor (SiC particles)). The results clearly show the great tailoring ability of the proposed microstructural model/processing routes applied to the development of innovative, low-cost, self-lubricating composites presenting low friction coefficient associated with high mechanical strength and wear resistance. Moreover, the optimized processing parameters produced outstanding new iron-based self- lubricating composites as illustrated in Table 3.1.

References

1. Cannaday, M.L., Polycarpou, A.A.: Tribology of unfilled and filled polymeric surfaces in refrigerant environment for compressor application. Tribol. Lett. **19**, 249–262 (2005)
2. Demas, N.G., Polycarpou, A.A.: Tribological investigation of cast iron air-conditioning compressor surfaces in CO$_2$ refrigerant. Tribol. Lett. **22**(3), 271–278 (2006)
3. Lee, Y.Z., Oh, S.D.: Friction and wear of the rotary compressor vane–roller surfaces for several sliding conditions. Wear. **255**, 1168–1173 (2003)
4. Solzak, T.A., Polycarpou, A.A.: Tribology of WC/C coatings for use in oil-less piston-type compressors. Surf. Coat. Technol. **201**, 4260–4265 (2006)
5. Pergande, S.R., Polycarpou, A.A., Conry, T.F.: Nanomechanical properties of aluminum 390-T6 rough surfaces undergoing tribological testing. J. Tribol. Trans. ASME. **126**, 573–582 (2004)

6. Oliveira Jr., M.M., Hammes, G., Binder, C., Klein, A.N., de Mello, J.D.B.: Solid lubrication in fluid film lubrication. Lubrication Science. **30**, 102–115 (2018)

7. Lancaster, J.K.: Solid lubricants. In: Booser, E.R. (ed.) CRC Handbook of Lubrication: Theory and Practice of Tribology Theory and design, vol. II, pp. 269–290 (1). CRC Press, Boca Raton (1984)

8. Sliney, H.E.: Solid lubricant materials for high temperatures: a review. Tribol. Int. **15**, 293–302 (1982)

9. Lansdown, A.R. Molybdenum disulphide lubrication. In: Dowson, D. (Ed.) Tribology series, vol. 35. Elsevier, Amsterdam (1999)

10. Brookes, C.A., Brookes, E.J.: Diamond on perspective. A review of mechanical properties of natural diamond. Diamond Relat. Mater. **1**, 13–17 (1991)

11. Donnet, C., Erdemir, A.: Historical developments and new trends in tribological and solid lubricant coatings. Surf. Coat. Technol. **180/181**, 76–84 (2004)

12. De Mello, J.D.B., Binder, R.: A methodology to determine surface durability in multifunctional coatings applied to soft substrates. Tribol. Int. **39**, 769–773 (2006)

13. De Mello, J.D.B., Binder, R., Demas, N.G., Polycarpou, A.A.: Effect of the actual environment present in hermetic compressors on the tribological behaviour of a Si rich multifunctional DLC coating. Wear. **267**, 907–915 (2009)

14. Bhushan, B. (ed.): Modern Tribology Handbook, vol. II. CRC Press, Boca Raton (2001)

15. Erdemir, A.: In: Bhushan, B. (ed.) Modern Tribology Handbook, vol. II, pp. 787–825. CRC Press, Boca Raton (2001)

16. Kimura, Y., Wakabayashi, T., Okada, K., Wada, T., Nishikawa, H.: Boron nitride as a lubricant additive. Wear. **232**, 199–206 (1999)

17. Erdemir, A.: Review of engineered tribological interfaces for improved boundary lubrication. Tribol. Int. **38**(3), 249–256 (2005)

18. Rapoport, L., Feldman, Y., Homyonfer, M., Cohen, H., Sloan, J., Hutchison, J.L., Tenne, R.: Inorganic fullerene-like material as additives to lubricants: structure-function relationship. Wear. **225–229**, 975–982 (1999)

19. Joly-Pottuz, L., Dassenoy, F., Belin, M., Vacher, B., Martin, J.M., Fleischer, N.: Ultralow-friction and wear properties of IF-WS$_2$ under boundary lubrication. Tribol. Lett. **18**(4), 477–485 (2005)

20. Tontini, G., Semione, G.D.L., Bernardi, C., Binder, R., de Mello, J.D.B., Drago, V.: Synthesis of nanostructured flower-like MoS$_2$ and its friction properties as additive in lubricating oils. Indust. Lubr. Tribol. **68**(6), 658–664 (2016)

21. Pacheco, F.G., Oliveira Jr, M.M., Santos, A.P., Costa, H.L., de Mello, J.D. B., Furtado, C.A.: Tribological evaluation of carbon nanotubes as additives in palm biolubricants. Submitted to Lubricants (2017)

22. Pauleau, Y., Thièry, F.: Deposition and characterization of nanostructured metalycarbon composite films. Surf. Coat. Technol. **180–181**, 313–322 (2004)

23. Erdemir, A.: Review of engineered tribological interfaces for improved boundary lubrication. Tribol. Int. **38**, 249–256 (2005)

24. Kato, H., Takama, M., Iwai, Y., Washida, K., Sasaki, Y.: Wear and mechanical properties of sintered copper–tin composites containing graphite or molybdenum disulfide. Wear. **255**, 573–578 (2003)

25. Dangsheng, X.: Lubrication behaviour of Ni–Cr-based alloys containing MoS$_2$ at high temperature. Wear. **251**, 1094–1099 (2001)

26. Huang, C., Du, L., Zhang, W.: Effects of solid lubricant content on the microstructure and properties of NiCr/Cr$_3$C$_2$–BaF$_2$·CaF$_2$ composite coatings. J. Alloys Compd. **479**, 777–784 (2009)

27. Zhu, S., Bi, Q., Yang, J., Liu, W., Xue, Q.: Effect of particle size on tribological behaviour of Ni$_3$Al matrix high temperature self-lubricating composites. Tribol. Int. **44**, 1800–1809 (2011)

28. Reeves, C.J., Menezes, P.L., Lovell, M.R., Jen, T.C.: The influence of surface roughness and particulate size on the tribological performance of bio-based multi-functional hybrid lubricants. Tribol. Int. **88**, 40–55 (2015)

29. Zhang, D., Lin, P., Dong, G., Zen, Q.: Mechanical and tribological properties of self-lubricating laminated composites with flexible design. Mater. Des. **50**, 830–838 (2013)
30. Burris, D.L., Sawyer, W.G.: A low friction and ultra-low wear rate PEEK/PTFE composite. Wear. **261**, 410–418 (2006)
31. Ouyang, J.H.: Microstructure and tribological properties of $ZrO_2(Y_2O_3)$ matrix composites doped with different solid lubricants from room temperature to 800 °C. Wear. **267**, 1353–1360 (2009)
32. Chen, B., Bi, Q., Yang, J., Xia, Y., Hao, J.: Tribological properties of solid lubricants (graphite, h-BN) for Cu-based P/M friction composites. Tribol. Int. **41**, 1145–1152 (2008)
33. Moghadam, A.D., Omrani, E., Menezes, P.L., Rohatgi, P.K.: Mechanical and tribological properties of self-lubricating metal matrix nanocomposites reinforced by carbon nanotubes (CNTs) and graphene: a review. Compos. Part B Eng. **77**, 402–420 (2015)
34. Tsuya, Y., Shimura, H., Umeda, K.: A study of the properties of copper and copper- tin base self-lubricating composites. Wear. **22**, 143–162 (1972)
35. Liu, E.R., Wang, W., Gao, Y., Jia, J.: Tribological properties of Ni-based self-lubricating composites with addition of silver and molybdenum disulfide. Tribol. Int. **57**, 235–241 (2013)
36. Binder, C., Hammes, G., Schroeder, R.M., Klein, A.N., de Mello, J.D.B., Binder, R.: 'Fine tuned' steels point the way to focused future. Met. Powder Rep. **65**, 29–37 (2010)
37. Mahathanabodee, S., Palathai, T., Raadnui, S., Tongsri, R., Sombatsompop, N.: Effects of hexagonal boron nitride and sintering temperature on mechanical and tribological properties of SS316L/h-BN composites. Mater. Des. **46**, 588–597 (2013)
38. de Mello, J.D.B., Binder, R., Klein, A.N., Hutchings, I.M.: Effect of compaction pressure and powder grade on microstructure and hardness of steam oxidised sintered iron. Powder Metall. **44**, 53–61 (2001)
39. de Mello, J.D.B., Hutchings, I.M.: Effect of processing parameters on the surface durability of steam-oxidized sintered iron. Wear. **250**, 435–448 (2001)
40. Ahn, H.S., Kim, J.Y., Lim, D.S.: Tribological behaviour of plasma-sprayed zirconia. Wear. **203**, 77–87 (1997)
41. PM Design Center of Metal Powder Industries Federation: Conventional Powdered Metal Components, 17 p (2012)
42. Tamura, S., Aizawa, T., Mitzuno, T., Kihara, J.: Steel powder compaction analysis. Int. J. Powder Metall. **34**, 50–59 (1998)
43. Al-Qureshi, H.A., Galiotto, A., Klein, A.N.: On the mechanics of cold die compaction for powder metallurgy. J. Mater. Process. Technol. **166**, 135–143 (2005)
44. Pavanati, H.C., Maliska, A.M., Klein, A.N., Muzart, J.L.R.: Comparative study of porosity and pores morphology of unalloyed iron sintered in furnace and plasma reactor. Mater. Res. **10**(1), 87–93 (2007)
45. Hammes, G., Schroeder, R.M., Binder, C., Klein, A.N., de Mello, J.D.B.: Effect of double pressing/double sintering on the sliding wear of self-lubricating sintered composites. Tribol. Int. **70**, 119–127 (2014)
46. Milligan, D., et al.: Materials properties of heat treated double pressed/sintered P/M steels in comparison to warm compacted/sinterhardened materials. In: PM^{2}TEC Advances in Powder Metallurgy and Particulate Materials, vol. 4, pp. 130–137 (2002)
47. James, B., et al.: Optimized double press-double sinter powder metallurgy method. US Patent 5,080,712, 1992
48. German, R.M.: Powder Metallurgy and Particulate Materials Processing, 1st edn, p. 528. Metal Powder Industries Federation, Princeton (2005)
49. German, R.M.: Powder Injection Molding, p. 521. Metal Powder Industries Federation, Princeton (1990)
50. Machado, R., Ristow, Jr., W., Klein, A.N., Muzart, J.L.R., et al.: Industrial plasma reactor for plasma assisted thermal debinding of powder injection molded parts. US Patent US7,718,919B2, PCT (WO 2006012718) and INPI (PI-0403536-4), 2010

51. Wendhausen, P.A.P., Fusao, D., Klein, A.N., Muzart, J.L.R., et al.: Plasma assisted debinding and sintering: process and equipment. In: Proceeding of the Powder Metallurgy World Congress & Exhibition, EURO PM2004, Vienna, vol. 4, pp. 37–142 (2004)
52. Klein, A.N., Muzart, J.L.R, et al.: Process for removal of binders from parts produced by powder injection moulding. US Patent US 6,579,493 B1, 2003
53. Klein, A.N., Binder, C., Hammes, G., de Mello, J.D.B., Ristow, W., Binder, R.: Self lubricating sintered steels with high mechanical resistance obtained via in situ formation of solid lubricant particles during sintering. In: Proceedings of EURO PM2009, vol. 1, pp. 191–196 (2009)
54. Binder, R., Klein, A.N., Binder, C., Hammes, G., Parucker, M.L., Ristow Jr., W.: Composicao metalurgica de materiais particulados, produto sinterizado autolubrificante e processo de obtencao de produtos sinterizados autolubrificantes. Patent application, PI 0803956-9, INPI, Brazil, 2008
55. Binder R., Binder, C., Ristow Jr., W., Klein, A.N.: Composition of particulate materials for forming self-lubricating products in sintered steels, product in self-lubricating sintered steel and process for obtaining self-lubricating products in sintered steel, PI0805606-Brazil; US 20110286873A1-USA; International Number: WO 2010/069020 A2-Europe; CN102497948A-China; JP 2012-512320-Japan; 10-2011-0110179-South Korea; SG 172168 A1-Singapore, TW 201034773 A1-Taiwan 2008
56. Lancaster, J.K.: Solid lubricants. In: Booser, E.R. (ed.) CRC Handbook of Lubrication, Theory and Practice of Tribology Theory and design, vol. II. CRC Press, Boca Raton (1984)
57. Xua, J., Zhang, R., Chena, P., Shena, D., Yea, X., Ge, S.: Mechanism of formation and electrochemical performance of carbide-derived carbons obtained from different carbides. Carbon. **64**, 444–455 (2013)
58. Totten, G. (ed.): Steel Heat Treatment: Metallurgy and Technologies, p. 191. CRC Press, Boca Raton (2007)
59. Binder, C., Bendo, T., Pereira, R. V., Hammes, G., de Mello, J.D.B, Klein, A.N.: Influence of the SiC content and sintering temperature on the microstructure, mechanical properties and friction behaviour of sintered self-lubricating composites. Powder Metallurgy. **59**, 1–10 (2016). https://doi.org/10.1080/00325899.2016.1250036
60. Callister Jr., W.D.: Fundamentals of Materials Science and Engineering, p. 552. Wiley, New York (2001)
61. Binder, C.: Desenvolvimento de novos tipos de aços sinterizados autolubrificantes a seco com elevada resistência mecânica aliada a baixo coeficiente de atrito via moldagem de pós por injeção. Ph.D. Thesis, Federal University of Santa Catarina, Brazil, 178 p. In Portuguese (2009)
62. ASM: ASM Handbook, Volume 1: Properties and Selection: Irons, Steels, and High-Performance Alloys, vol. 1. ASM International, Materials Park. 1063 p (1990)
63. Thelning, K.E: Steels and its heat treatment, 2nd edn. Butterworths, London. 450 p (1984)
64. Rohatgi, P.K., Ray, S., Liu, Y.: Tribological properties of metal matrix graphite particle composites. Int. Mater. Rev. **37**, 129–149 (1992)
65. Matthews, M.J., Pimenta, M.A., Dresselhaus, G., Dresselhaus, M.S., Endo, M.: Origin of dispersive effects of the Raman D-band in disordered carbon materials. Phys. Rev. B. **59**, R6585 (1999)
66. Cançado, L.G., Pimenta, M.A., Saito, R., et al.: Stokes and anti-stokes double resonance Raman scattering in two-dimensional graphite. Phys. Rev. B. **66**, 035415 (2002)
67. Ferrari, A.C., Meyer, V., Scardaci, C., et al.: Raman spectrum of graphene and graphene layers. Phys. Rev. Lett. **97**, 187401 (2006)
68. Ferrari, A.C.: Raman spectroscopy of graphene and graphite: disorder, electron–phonon coupling, doping and non adiabatic effects. Solid State Commun. **143**, 47–57 (2007)
69. de Mello, J.D.B., Binder, C., Binder, R., Klein, A.N.: Effect of precursor content and sintering temperature on the scuffing resistance of sintered self-lubricating steel. Wear. **271**, 1862–1867 (2011)
70. Ferrari, A.C., Robertson, J.: Interpretation of Raman spectra of disordered and amorphous carbon. Phys. Rev. B. **61**, 14095–14107 (2000)

71. Lespade, P., Marchand, A., Couzi, M., Cruege, F.: Caracterisation de materiaux carbones par microspectrometrie Raman. Carbon. **22**, 375–385 (1984)
72. Binder, C., Bendo, T., Hammes, G., Neves, G.O., de Mello, J.D.B, Klein, A.N., Binder, R.: Structure and properties of in situ generated 2D turbostratic graphite nodules. Carbon. **124**, 685–692 (2017)
73. Pimenta, M.A., Dresselhaus, G., Dresselhaus, M.S., Cançado, L.G., Jorio, A., Saito, R.: Studying disorder in graphite-based systems by Raman spectroscopy. Phys. Chem. Chem. Phys. **9**, 1276–1291 (2007)
74. Le Roux, H.: An electron diffraction analysis of turbostratic graphite in cemented carbides. Acta Metall. **33**, 309–315 (1985)
75. Karthik, C., Kane, J., Butt, D.P., Windes, W.E., Ubic, R.: Microstructural characterization of next generation nuclear graphites. Microsc. Microanal. **18**, 272–278 (2012)
76. Campos, K.R.: Caracterização tribológica da lubrificação sólida. Ph.D. Thesis, Universidade Federal de Uberlândia, Brazil, 2012, 162 p. In Portuguese (2012)
77. Lim, S.C., Brunton, J.H.: The unlubricated wear of sintered iron. Wear. **113**, 371–382 (1986)
78. Campos, K.R., Kapsa, P., Binder, C., Binder, R., Klein, A.N., de Mello, J.D.B.: Tribological evaluation of self-lubricating sintered steels. Wear. **332–333**, 932–940 (2015)
79. Keller, J., Fridrici, V., Kapsa, P.H., Huard, J.F.: Surface topography and tribology of cast iron in boundary lubrication. Tribol. Int. **42**, 1011–1018 (2009)
80. Zum Gahr, K.H.: Microstructure and Wear of Materials Tribolology Series, vol. 10. Elsevier, Amsterdam (1987.) 560 pp
81. Babu, S.S.: Acicular ferrite and bainite in steels. Ph.D. Thesis, University of Cambridge, UK (1992)
82. de Mello, J.D.B., Binder, C., Hammes, G., Klein, A.N.: Effect of the metallic matrix on the sliding wear of plasma assisted debinded and sintered MIM self-lubricating steel. Wear. **301**, 648–655 (2013)
83. Beattie, I.R., Gibson, T.R.J.: J. Chem. Soc. A. **6**, 980 (1970)
84. Oh, S.J., Cook, D.C., Townsend, H.E.: Characterization of iron oxides commonly formed as corrosion product on steel. Hyperfine Interact. **112**, 59–65 (1998)
85. Crockett, R.M., Derendinger, M.P., Hug, P.L., Roos, S.: Wear and electrical resistance on diesel lubricated surfaces undergoing reciprocating sliding. Tribol. Lett. **16**, 187–194 (2004)
86. Ouyang, M., Hiraoka, H.: Structure and magnetic properties of iron oxide films deposited by excimer laser ablation of a metal-containing polymer. Mater. Res. Bull. **32**, 1099–1107 (1997)